Technical Briefs

An Infinite Dimensional Distributed Base Controller for Regulation of Flexible Robot Arms

Nader Jalili
Associate Mem. ASME
Assistant Professor,
Robotics and Mechatronics Laboratory, Department of
Mechanical Engineering, Clemson University,
Clemson, SC 29634-0921
e-mail: jalili@clemson.edu.

An exponentially stable variable structure controller is presented for regulation of the angular displacement of a one-link flexible robot arm, while simultaneously stabilizing vibration transient in the arm. By properly selecting the sliding hyperplane, the governing equations which form a nonhomogenous boundary value problem are converted to homogenous ones, and hence, analytically solvable. The controller is then designed based on the original infinite dimensional distributed system which, in turn, removes some disadvantages associated with the truncated-model-base controllers. Utilizing only the arm base angular position and tip deflection measurements, an on-line perturbation estimation routine is introduced to overcome the measurement imperfections and ever-present unmodeled dynamics. Depending on the composition of the controller, some favorable features appear such as elimination of control spillovers, controller convergence at finite time, suppression of residual oscillations and simplicity of the control implementation. Numerical simulations along with experimental results are provided to demonstrate and validate the effectiveness of the proposed controller. [DOI: 10.1115/1.1408608]

1 Introduction

In recent years, the demands for high-speed performance, low energy consumption and low cost have been motivating the use of lightweight robot manipulators in industrial applications. The rigid structure of current industrial manipulators has made compliance impossible and limited the robotics use in automation tasks. The use of lightweight flexible links, however, has led to a challenging problem in end-point trajectory control. Due to the flexibility distributed along the robot arms, an improved control scheme is required to track the desired trajectory while simultaneously suppressing the vibrational transients in the arm.

This control problem has attracted significant attention in the literature. A flexible manipulator control must achieve the motion

tracking objectives (similar to that of rigid one) while stabilizing the transient vibrations in the arm. Several control methods have been developed for flexible arms: optimal control [1,2]; finite element approach [3,4]; model reference adaptive control [5]; adaptive non-linear boundary control [6]; and several other techniques including variable structure control (VSC) methods [7–9]. Most of these methods concentrate on model-based controllers design. Some of these controllers, however, may not be easy to implement due to the uncertainties in the design model, large variations of the loads, ignored high frequency dynamics and high order of the designed controllers. In view of these methods, VSC is particularly attractive due to its simplicity of implementation and robustness to parameter uncertainties. Successful applications of this method in practical systems are numerous ([10–12] are just a few).

Generally, a flexible robot is governed by partial differential equations (PDE) as a system of distributed-parameter and therefore possesses infinite number of dimensions. Due to the complexity of these equations and in order to facilitate the application of control strategies, discretization techniques are typically used to construct a finite-dimensional reduced model. Based on the resulting approximate model (assumed mode model (AMM) or finite element method (FEM), for instance) several controller design approaches are then applied [4,5], and [13].

The problem associated with these model-based controllers is the truncation procedure used in the approximation. Due to ignored high frequency dynamics (related to control spillovers) and high order of the designed controller (related to increased number of flexible modes utilized in the model), severe limitations occur in implementation of these controllers. To overcome these shortfalls, alternative approaches based on infinite dimensional distributed (IDD) partial differential models of flexible arms have been developed. A direct strain feedback control strategy was proposed to control vibration of flexible arm [9], while an exponentially stable VSC controller is utilized for flexible robot systems with translational base [14].

A common difficulty appears in all these IDD-base controller design, which is the complexity of the control implementation. For instance, the control strategy developed in [14] requires measurements of displacement, velocity and acceleration of the arm tip as well as the shear force at the root end of the link. Although the VSC controller is inherently insensitive to parameter variations, feasible measurements are required for a successful implementation of the controller. This is the reason why experimental verification of these algorithms is progressing with a much slower pace than the theoretical compartment. For more complex flexible systems (multi-link arms, for instance) these approaches become very hard in practical implementation.

It is, therefore, highly desirable to seek a simple and yet practical technique for control of flexible arms. To this end, an improved IDD-base controller is proposed to eliminate the disadvantages associated with the traditional truncated-model-base controllers. It is specifically intended to further relax the measurement requirements for the flexible arm and simplify the controller design. Only the tip deflection and angular position of the flexible
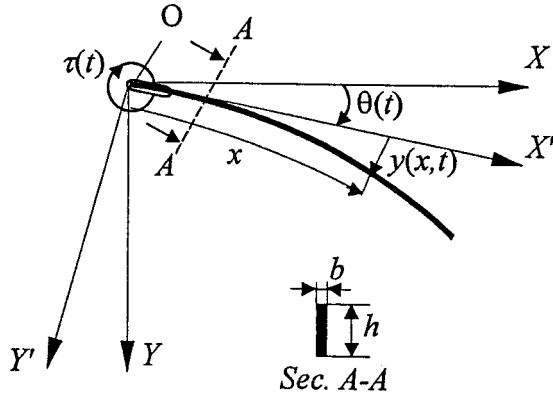
Fig. 1   Flexible arm in the horizontal plane with its kinematics of deformation

arm are required to develop the new controller proposed here. The remaining measurements, the ever-present unmodeled dynamics and other parameter uncertainties are all combined to a single term and estimated through an on-line perturbation estimation process [15,16]. This additional perturbation estimation will compromise the robustness and trajectory tracking accuracy.

2   Mathematical Modeling

We consider regulation of the angular displacement of a one-link flexible arm. As shown in Fig. 1, one end of the arm is free and the other end is rigidly attached to a vertical gear shaft, driven by a DC motor. Thus, the effect of gravity is neglected. Uniform cross section is considered for the arm, and we make the Euler-Bernoulli assumptions. The control torque τ, acting on the output shaft, is normal to the plane of motion. Viscous frictions and the ever-present unmodeled dynamics of the motor compartment are to be compensated via a perturbation estimation process, as explained later in the text.

Since the dynamic system considered here has been utilized in literature quite often, we present only the resulting partial differential equation (PDE) of the system and refer the interested readers to [17,18] for detailed derivations. The system is governed by

$$I_t\ddot{\theta}(t) + \rho\int_0^L x\ddot{y}(x,t)dx = \tau \tag{1}$$

$$\rho[x\ddot{\theta}(t) + \ddot{y}(x,t)] + EIy'''(x,t) = 0 \tag{2}$$

with the corresponding boundary conditions

$$y(0,t) = 0, \tag{3}$$

$$y'(0,t) = 0, \tag{4}$$

$$y''(L,t) = 0, \tag{5}$$

$$y'''(L,t) = 0 \tag{6}$$

where ρ is the arm liner mass density, L is the arm length, E is the Young's modulus of elasticity, I is the cross-sectional moment of inertia, I_h is the equivalent mass moment of inertia at the root end of the arm, and $I_t = I_h + \rho L^3/3$ is the total inertia. Equation (1) represents the motion of the arm base, while (2) describes the vibration of the arm.

Using global variable

$$z(x,t) = x\theta(t) + y(x,t) \tag{7}$$

the differential equations and boundary conditions can be expressed in the global coordinates as

$$I_h\ddot{\theta}(t) + \rho\int_0^L x\ddot{z}(x,t)dx = \tau \tag{8}$$

$$\rho\ddot{z}(x,t) + EIz''''(x,t) = 0 \tag{9}$$

with the corresponding boundary conditions

$$z(0,t) = 0, \tag{10}$$

$$z'(0,t) = \theta(t), \tag{11}$$

$$z''(L,t) = 0, \tag{12}$$

$$z'''(L,t) = 0 \tag{13}$$

Clearly, the arm vibration equation (9) is a homogenous PDE but the boundary conditions (10–13) are nonhomogenous. Therefore, the closed-form solution is very tedious to obtain, if not impossible. Using the application of VSC, these equations and their associated boundary conditions can be converted to a homogenous boundary value problem, as discussed next.

3   Variable Structure Controller

The control objective is to track the arm angular displacement from an initial angle, $\theta_d = \theta(0)$, to zero position, $\theta(t\to\infty) = 0$, while minimizing the flexible arm oscillations. To achieve the control insensitivity against modeling uncertainties, the nonlinear control routine of Sliding Mode Control with an additional Perturbation Estimation (SMCPE) compartment is adopted here [15,16]. The method of SMCPE presented in [15] has many attractive features, but is suffers from the disadvantages associated with the truncated-model-base controllers. On the other hand, the IDD-base controller design, proposed in [14], has practical limitations due to its measurement requirements in addition to the complex control law. We propose a new scheme to overcome these shortfalls.

3.1   Controller Design.   Initiating from the idea of IDD-base controller, we propose a new controller design approach in which an on-line perturbation estimation mechanism is integrated with the controller to relax the measurement requirements. As utilized in [14], for the tip vibration suppression, it is further required that the sliding surface enable the transformation of nonhomogenous boundary conditions (10–13) to homogenous ones. To simultaneously satisfy vibration suppression and robustness requirements, the sliding hyperplane is selected as a combination of tracking (regulation) error and arm flexible vibration as

$$s = \dot{w} + \sigma w \tag{14}$$

where $\sigma > 0$ is a control parameter and

$$w = \theta(t) + \frac{\mu}{L}z(L,t) \tag{15}$$

with the scalar μ being selected later. When $\mu = 0$, controller (14) reduces to sliding variable for rigid-link manipulators [16,19]. The motivation for such a sliding variable is to provide a suitable boundary condition for solving the beam equation (9) as will be discussed next.

Theorem 3.1   For the system described by (1) and (9), if the variable structure controller is given by

$$\tau = \psi_{est} + \frac{I_t}{1+\mu}\left(-k\,\mathrm{sgn}(s) - Ps - \frac{\mu}{L}\ddot{y}(L,t)\right.$$

$$\left. -\sigma(1+\mu)\dot{\theta} - \frac{\sigma\mu}{L}\dot{y}(L,t)\right) \tag{16}$$

where ψ_{ext} is an estimate of the beam flexibility effect

$$\psi = \rho\int_0^L x\ddot{y}(x,t)dx, \tag{17}$$

k and P are positive scalars, $k \geq (1+\mu)|\psi-\psi_{est}|/I_t$, $-1.2 < \mu < -0.45$, $\mu \neq -1$ and

$$\text{sgn}(s) = \begin{cases} 1 & s>0 \\ -1 & s<0 \end{cases} \tag{18}$$

then the system's motion will first reach the sliding mode $s=0$ in a finite time, and consequently converge to the equilibrium position $w(x,t)=0$ exponentially with a time-constant $1/\sigma$

Proof: Selecting Lyapunov function candidate $V = I_t s^2/2$, its time derivative is given by

$$\dot{V} = I_t s \dot{s} \tag{19}$$

From Eq. (7), (14), and (15), we have

$$\dot{s} = \ddot{w} + \sigma \dot{w} = (1+\mu)\ddot{\theta} + \frac{\mu}{L}\ddot{y}(L,t) + \sigma\left[\dot{\theta} + \frac{\mu}{L}\dot{z}(L,t)\right] \tag{20}$$

Substituting (20) into (19) and utilizing (7) yields

$$\dot{V} = s\left[I_t(1+\mu)\ddot{\theta} + I_t\frac{\mu}{L}\ddot{y}(L,t) + I_t\sigma(1+\mu)\dot{\theta} + I_t\sigma\frac{\mu}{L}\dot{y}(L,t)\right] \tag{21}$$

Noting (1), Eq. (21) becomes

$$\dot{V} = s\left\{I_t(1+\mu)\left[\frac{\tau}{I_t} - \frac{\rho}{I_t}\int_0^L x\ddot{y}(x,t)dx\right]\right.$$
$$\left. + I_t\frac{\mu}{L}\ddot{y}(L,t) + I_t\sigma(1+\mu)\dot{\theta} + I_t\sigma\frac{\mu}{L}\dot{y}(L,t)\right\} \tag{22}$$

Substituting controller (16) into (22) yields

$$\dot{V} = s\{(1+\mu)(\psi_{est} - \psi) - I_t k \,\text{sgn}(s) - I_t P_s\} \tag{23}$$

Invoking condition $k \geq (1+\mu)|\psi - \psi_{est}|/I_t$, Eq. (23) reduces to

$$\dot{V} \leq -I_t k|s| \tag{24}$$

As shown in [20], inequality (24) implies that the system will reach the sliding mode $s=0$ in a finite time, which is smaller than $|s(t=0)|/k$, and then remain in the sliding mode. Therefore, from (14), the system's motion, after reaching the sliding mode, will slide along $s=0$ toward $w=0$ exponentially with a time constant equal to $1/\sigma$.

It should be noted that condition $k \geq (1+\mu)|\psi - \psi_{est}|/I_t$ is based on the assumption that $|\psi - \psi_{est}| \leq \eta\psi_{est}$ where η is experimentally determined [21]. In order to assure robustness, k is selected as

$$k = \eta(1+\mu)\psi_{est}/I_t \tag{25}$$

The discontinuity in the controller due to the signum function can be smoothened by replacing it with the saturation function

$$\text{sat}(s) = \begin{cases} s/\varepsilon & |s| \leq \varepsilon \\ \text{sgn}(s) & |s| > \varepsilon \end{cases} \tag{26}$$

in order to avoid control chatter [22]. However, if the forced oscillations of the s-dynamic display high frequencies, then the corresponding (saturation function) control component manifest equally high frequency dither, which is not desirable either. Therefore, a "low pass filter" mode, P in controller (16), was introduced to subdue the effects of high frequency components [15]. Once the system enters the sliding phase, the s-dynamics take the form of a low pass filter against $|\psi - \psi_{est}|$ as (see Eq. (23))

$$\dot{s} + (P + k/\varepsilon)s = \frac{1+\mu}{I_t}|\psi - \psi_{est}| \tag{27}$$

We have proven that the system's motion converges to $w=0$ exponentially. To prove the exponential stability of the closed-loop system, it will be sufficient to show that the flexible arm stops at the final equilibrium position $z(x,t)=0$ provided that $w=0$ [14]. Since $\omega \to 0$ as $t \to \infty$, based on (14) same holds for θ (i.e., $\theta \to 0$). Notice, from (15), $w=0$ implies that

$$\theta(t) = -\frac{\mu}{L}z(L,t) \tag{28}$$

Substituting (28) into boundary condition (11), transforms the nonhomogenous boundary value problem (9–13) into a homogenous one. Specifically, the boundary condition (11) is recast in the homogenous form of

$$z'(0,t) = -\frac{\mu}{L}z(L,t) \tag{29}$$

which fulfills our objective. By properly selecting variable μ, it is shown, next, that the arm can be stopped at the final position.

3.2 Solution to Homogenous Boundary Value Problem. In the derivation of the controller, we shall assume that the system can be variable-separated, i.e., $z(x,t)$ can be represented by

$$z(x,t) = \phi(x)Q(t) \tag{30}$$

where $\phi(x)$ is the transverse modal shape of the flexible arm and $Q(t)$ is the corresponding generalized coordinate. Note that the derivation of the controller does not require any modal reduction, i.e., the controller, theoretically, can handle the original infinite-dimensional system [14].

Substituting Eq. (30) into (9) yields

$$\frac{\phi''''}{\phi}\frac{EI}{\rho} = -\frac{\ddot{Q}}{Q} \tag{31}$$

Consequently, we obtain two ordinary differential equations [18]

$$\ddot{Q}(t) + KQ(t) = 0 \tag{32}$$

$$\phi''''(x) = \frac{\rho}{EI}K\phi(x) \tag{33}$$

with the boundary conditions

$$\phi(0) = 0, \tag{34}$$

$$\phi'(0) = -\frac{\mu}{L}\phi(L), \tag{35}$$

$$\phi''(L) = 0, \tag{36}$$

$$\phi'''(L) = 0 \tag{37}$$

To solve this boundary value problem, we consider three possible options for K.

Case I: $K=0$. This yields the following expression for $\phi(x)$

$$\phi(x) = C_1 x^3 + C_2 x^2 + C_3 x + C_4 \tag{38}$$

To force $\phi(x)=0$, which will lead to $z(x,t)=0$, all the coefficients C_i ($i=1,\ldots,4$) must vanish. Utilizing this and Eq. (34)–(37), one can show that these conditions are satisfied if

$$\mu \neq -1 \tag{39}$$

Case II: $K<0$. By letting $K = -\omega^2$, Eq. (33) is written as

$$\phi''''(x) = -\left(\frac{\beta}{L}\right)^4\phi(x) \tag{40}$$

where $(\beta/L)^4 = \rho\omega^2/EI$. Noting $a = \sqrt{2}\beta/2L$ ($a \neq 0$), the general solution to Eq. (40) is of the form

$$\phi(x) = C_1 e^{ax}\sin(ax) + C_2 e^{ax}\cos(ax) + C_3 e^{-ax}\sin(ax)$$
$$+ C_4 e^{-ax}\cos(ax) \tag{41}$$

By substituting boundary conditions (34–37) into equation (41), a set of four homogenous linear algebraic equations in terms of coefficients C_i ($i=1,\ldots,4$) is rendered. Using MAPLE software package [23], the determinant of the coefficients matrix is found to be

$$\Delta = 16a^6 \left\{ \left[\frac{\cos(aL)\sinh(aL) + \sin(aL)\cosh(aL)}{aL} \right] \mu \right.$$
$$\left. + \cosh^2(aL) + \cos^2(aL) \right\} \qquad (42)$$

In order to force $C_i = 0$, we need to show that $\Delta \neq 0$. Using MAPLE package, it can be shown that condition $-1.2 < \mu < 35$ will render $\Delta > 0$ regardless of the value of aL (notice, $aL \neq 0$ in this case).

Case III: $K > 0$. Letting $K = \omega^2$, the general solution to (33) can be expressed in the form

$$\phi(x) = C_1 \cos(\beta x/L) + C_2 \cosh(\beta x/L)$$
$$+ C_3 \sin(\beta x/L) + C_4 \sinh(\beta x/L) \qquad (43)$$

Similarly, substituting boundary conditions (34–37) into Eq. (43) and taking the determinant of the coefficients yields

$$\Delta = -\frac{2\beta^6}{L^6} \left\{ \frac{(\sin\beta + \sinh\beta)}{\beta} \mu + \cosh\beta\cos\beta + 1 \right\} \qquad (44)$$

Utilizing MAPLE again, it can be shown that regardless of value of $\mu (\mu \neq 0)$ in this case, $\Delta \neq 0$. Notice, in this case $\beta \neq 0$. The values of $\mu > 2.3$ will render $\Delta < 0$ and values of $\mu < -0.45$ will result $\Delta > 0$.

Recalling all the three cases, one can see if μ satisfies the inequality

$$-1.2 < \mu < -0.45, \quad \mu \neq -1 \qquad (45)$$

then $\Delta > 0$, and that results in $\phi(x) = 0$ and ultimately $z(x,t) = 0$. This is the same condition given in Theorem 3.1. Now, we can conclude that $w = 0$ implies that the flexible beam and consequently arm angular displacement stop at the final equilibrium position $z(x,t) = 0$ and $\theta(t) = 0$. Consequently, because $w \rightarrow 0$ exponentially in the sliding mode, the system motions also converges to $z(x,t) = 0$ exponentially with time constant $1/\sigma$. This completes the proof. (QED)

Remark 3.1: The range of μ given in Eq. (45) may not be a complete solution. Analytically solving for μ from (42) and (44) is quite complicated. Consequently, Theorem 3.1 gives only a sufficient condition to stabilize the system.

4 Controller Implementation

In the preceding section, it was shown that by properly selecting control variable μ, the motion exponentially converges to $w = 0$ with a time-constant $1/\sigma$, while the arm stops in a finite time. Although, the discontinuity nature of the controller introduces a robustizing mechanism, we have further made the scheme insensitive to parametric variations and unmodeled dynamics by reducing the required measurements and hence easier control implementation. The remaining measurements and ever-present modeling imperfection effects have all been estimated through an on-line estimation process. To realize the variable structure controller (16), we need to feedback the following quantities: $\psi_{est}(t)$, $\theta(t)$, $\dot{\theta}(t)$, $y(L,t)$, $\dot{y}(L,t)$, and $\ddot{y}(L,t)$. As stated before, in order to simplify the control implementation and reduce the measurement effort, the effect of all uncertainties including flexibility effect ($\int_0^L x\ddot{y}(x,t)dx$) and the ever-present unmodeled dynamics is gathered into a single quantity named perturbation, ψ, as given by (17).

Noting (1), the perturbation term can be expressed as

$$\psi = \tau - I_t \ddot{\theta}(t) \qquad (46)$$

where requires the yet unknown control feedback τ. In order to resolve this dilemma of causality, the current value of control torque τ is replaced by the most recent control $\tau(t-\delta)$, where δ is the small time-step used for the loop closure. This replacement is justifiable in practice, since such algorithm is implemented on a

digital computer and the sampling speed is high enough to claim this. Also, in the absence of measurement noise, $\ddot{\theta}(t) \cong \ddot{\theta}_{cal}(t) = [\dot{\theta}(t) - \dot{\theta}(t-\delta)]/\delta$.

Therefore, an estimate of perturbation ψ is utilized as

$$\psi_{est} = \tau(t-\delta) - I_t \ddot{\theta}_{cal}(t) \qquad (47)$$

Alternatively, the bending moment of the beam at its base can be obtained as [17,18]

$$EIy''(0,t) = -\rho \int_0^L x\ddot{z}(x,t)dx \qquad (48)$$

Then, the flexibility term used in perturbation expression can be expressed as

$$\psi = \rho \int_0^L x\ddot{y}(x,t)dx = -EIy''(0,t) - \rho\ddot{\theta}(t)L^3/3 \qquad (49)$$

which can be measured in practice by attaching a strain gauge at the base of the flexible arm for $y''(0,t)$ and approximating $\ddot{\theta}(t)$ with $\ddot{\theta}_{cal}(t)$ as described above.

Due to the additional robustizing feature, perturbation estimation, the following approximations can be utilized at the control stage implementation (Section 6):

$$\ddot{y}(L,t) \cong \ddot{y}_{cal}(L,t) = [\dot{y}_{cal}(L,t) - \dot{y}(L,t-\delta)]/\delta,$$
$$\ddot{\theta}(t) \cong \ddot{\theta}_{cal}(t) = [\dot{\theta}_{cal}(t) - \dot{\theta}_{cal}(t-\delta)]/\delta, \qquad (50)$$

where

$$\dot{y}_{cal}(L,t) = [y(L,t) - y(L,t-\delta)]/\delta$$
$$\dot{\theta}_{cal}(t) = [\theta(t) - \theta(t-\delta)]/\delta. \qquad (51)$$

In practice and in the presence of measurement noise, appropriate filtering may be considered and combined with these approximate derivatives. This technique is referred to as "switched derivatives." This backward differences is shown to be effective when δ is selected small enough and the controller is run on a fast DSP [24,25]. Also, $\ddot{y}(L,t)$ can be obtained by attaching an accelerometer at arm tip position. All the required signals are therefore measurable by currently available sensor facilities and the controller is thus realizable in practice. Although these signals may be quite inaccurate, it should be pointed out that the signals, either by measurements or estimation, need not to be known very accurately since robust sliding control can be achieved if k is chosen large enough to cover the error existing in the measurement/signal estimation [10].

5 Numerical Simulations

In order to show the effectiveness of the proposed controller, a lightweight flexible arm is considered ($h \gg b$ in Fig. 1). For numerical results, we consider $\theta_d = \theta(0) = \pi/2$ for the initial arm base angle, with zero initial conditions for the rest of the state variables.

The system parameters are listed in Table 1. Utilizing assumed mode model, the arm vibration equation (9) is truncated to 3 modes and used in the simulations. It should be noted that the controller law, Eq. (16), is based on the original infinite dimensional equation, and this truncation is utilized only for simulation purposes.

We take the controller parameter $\mu = -0.66$, which satisfies inequality (45). The other control parameters are chosen as $P = 7.0$, $k = 5$, $\epsilon = 0.01$ and $\sigma = 0.8$. In practice, σ is selected for maximum tracking accuracy taking into account unmodeled dynamics and actuator hardware limitations [21]. Although such restrictions do not exist in simulations (i.e., ideal actuator, high sampling frequency and perfect measurements), this selection of σ was decided based on the actual experiment conditions (see Section 6).

Table 1   System parameters for numerical simulations and experimental setup

Properties	Symbol	Value	Unit
Arm Young's modulus	E	207×10^9	N/m^2
Arm thickness	b	0.0008	m
Arm height	h	0.02	m
Arm length	L	0.45	m
Arm linear mass density	ρ	$0.06/L$	Kg/m
Arm base inertia (including fixture, motor, camera and gearbox)	I_h	0.002	$Kg.m^2$
Gearbox ratio	N	14:1	-
Light source mass	-	0.05	Kg
Position sensor sensitivity	-	0.39	V/cm
Motor back EMF constant	K_b	0.0077	V/rad/sec
Motor torque constant	K_t	0.0077	N.m/amp
Armature resistance	R_a	2.6	Ohms
Armature inductance	L_a	0.18	mHenry
Encoder resolution	-	0.087	Deg/count

The sampling rate for the simulations is $\delta = 0.0005$ sec, while data are recorded at the rate of only 0.002 sec for plotting purpose. The system responses to the proposed control scheme are shown in Fig. 2. The arm base angular position reaches the desired position $\theta = 0$ in about 4–5 s, which is in agreement with the approximate settling time of $t_s = 4/\sigma$ (Fig. 2(a)). As soon as system reaches the sliding mode layer $|s| < \epsilon$ (Fig. 2(d)), the tip vibrations stop (Fig. 2(b)), which demonstrates the feasibility of the proposed control technique. The control torque exhibits some residual vibration as shown in Fig. 2(c). This residual oscillation is expected since the system motion is not forced to stay on $s = 0$ surface (instead it is forced to stay on $|s| < \epsilon$ when saturation function is used. The sliding variable s is also depicted in Fig. 2(d).

To better demonstrate the feature of the controller, the system responses are displayed when $\mu = 0$ (Fig. 3). As discussed, $\mu = 0$ corresponds to the sliding variable for the rigid-link. The undesirable oscillations at the arm tip are evident (see Figs. 3(b) and 3(c)).

6   Control Experiments

In order to better demonstrate the effectiveness of the controller, an experimental setup is constructed and used to verifying the numerical results and concepts discussed in the preceding sections. It is specifically intended to demonstrate the robustizing feature of the controller in the presence of unmodeled dynamics in the actuator (frictional torque in the motor), the arm payload and measurements imperfections.

6.1   Experimental Setup. The experimental setup is shown in Fig. 4. The arm is a slender beam made of stainless steel, with the same dimensions used in the simulations. The experimental setup parameters are listed in Table 1. One end of the arm is clamped to a solid clamping fixture, which is driven by a high quality DC servomotor. The motor drives a built-in gearbox ($N = 14:1$) whose output drives an anti-backlash gear. The anti-backlash gear, which is equipped with a precision encoder, is utilized for measuring the arm base angle as well as to eliminate the backlash. For tip deflection, a light source is attached to the tip of the arm which is detected by a camera mounted on the rotating base.

The DC motor can be modeled as a standard armature circuit. That is, the applied voltage v to the DC motor is

$$v = R_a i_a + L_a di_a/dt + K_b \dot{\theta}_m \tag{52}$$

where R_a is the armature resistance, L_a is the armature inductance, i_a is the armature current, K_b is the back-EMF (electro-
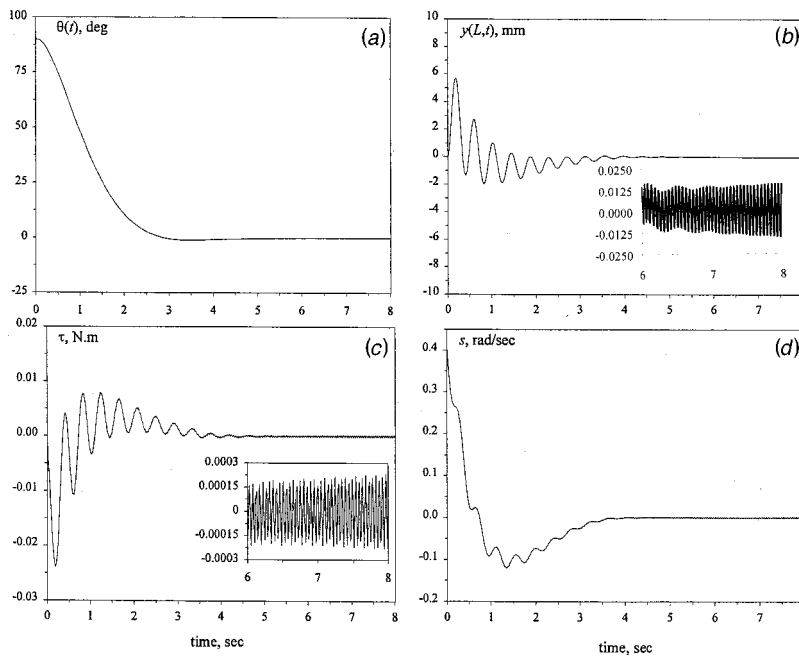
Fig. 2   Analytical system responses to controller with inclusion of arm flexibility, i.e., $\mu = -0.66$; (a) arm angular position, (b) arm tip deflection, (c) control torque, and (d) sliding variable s
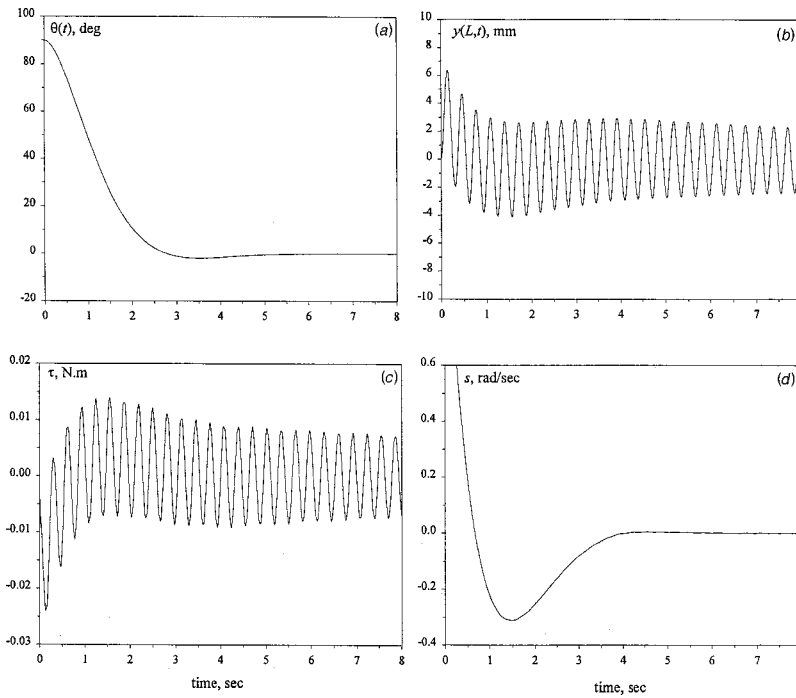
Fig. 3 Analytical system responses to controller without inclusion of arm flexibility, i.e., $\mu = 0$; (a) arm angular position, (b) arm tip deflection, (c) control torque, and (d) sliding variable s

motive-force) constant, and θ_m is the motor shaft position. The motor torque, τ_m, from the motor shaft with the torque constant K_t can be written as

$$\tau_m = K_t i_a \tag{53}$$

The motor dynamics thus become

$$I_e \ddot{\theta}_m + C_v \dot{\theta}_m + \tau_a = \tau_m = K_t i_a \tag{54}$$

where C_v is the equivalent damping constant of the motor, and $I_e = I_m + I_L/N^2$ is the equivalent inertia load including motor inertia, I_m, and gearbox, clamping frame and camera inertia, I_L. τ_a is the available torque from the motor shaft for the arm.

Utilizing the gearbox from the motor shaft to the output shaft and ignoring the motor electric time constant (L_a/R_a), one can relate the servomotor input voltage to the applied torque (acting on the arm) as

$$\tau = \frac{NK_t}{R_a} v - \left(C_v + \frac{K_t K_b}{R_a} \right) N^2 \dot{\theta} - I_h \ddot{\theta} \tag{55}$$

where $I_h = N^2 I_e$ is the equivalent inertia of the arm base used in the derivation of governing equations (see Eq. (1)). By substituting this torque into the control law, the reference input voltage V can be obtained for experiment.

6.2 Experimental Results on Regulation Control. As stated before, only arm base angular position and tip deflection are to be measured. The remaining required signals for the controller (16) are determined as explained in Section 4. The control torque is applied via a digital signal processor (DSP) with sampling rate of 10 kHz, while data are recorded at the rate 500 Hz (for plotting purpose only). The DSP runs the control routine in a single input-single output mode as a free standing CPU. Most of the computations and hardware commands are done on the DSP card. For this setup, a dedicated 500 MHz Pentium III serves as the host PC,

and a state-of-the-art dSPACE® DS1103 PPC controller board equipped with Motorola Power PC 604e at 333 MHz, 16 channels ADC, 12 channels DAC as microprocessor.

The experimental system responses are shown in Figs. 5 and 6 for similar cases discussed in the numerical simulation section. Figure 5 represents the system responses when controller (16) utilizes the flexible arm (i.e., $\mu = -0.66$). As seen, the arm base reaches the desired position (Fig. 5(a)), while tip deflection is simultaneously stopped (Fig. 5(b)). The good correspondence between analytical results (Fig. 2) and experimental findings (Fig. 5) is noticeable from vibration suppression characteristics point of view. It should be noted that the controller is based on the original governing equations, with arm base angular position and tip deflection measurements only. The unmodeled dynamics such as payload effect (due to the light source at tip, see Table 1), viscous friction (at the root end of the arm) are being compensated through the proposed on-line perturbation estimation routine.
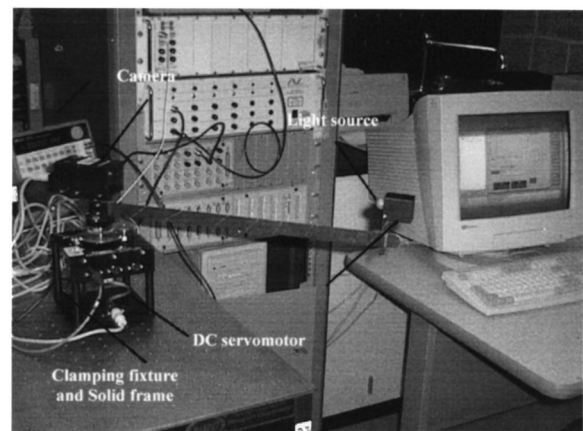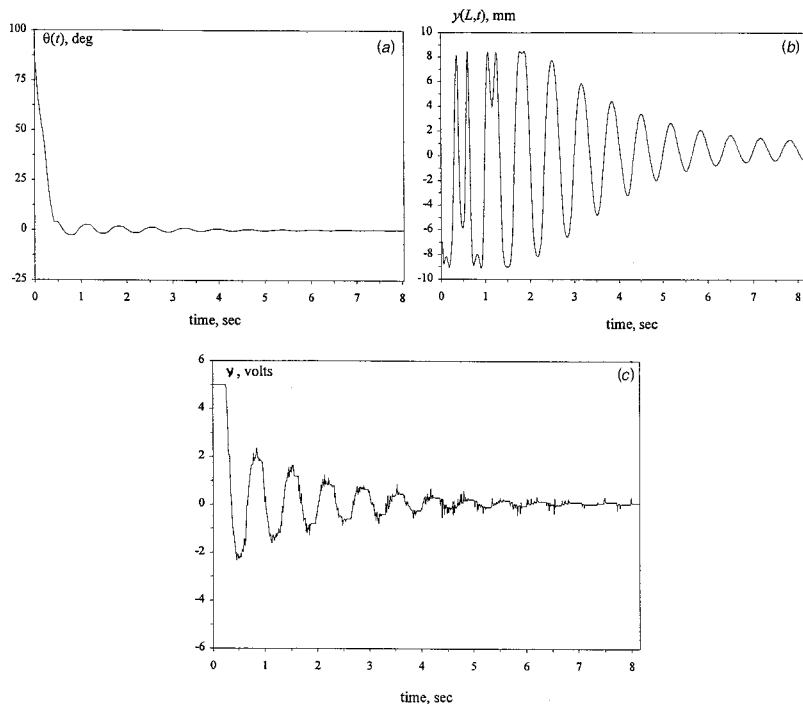

Fig. 4 The experimental device and setup configuration
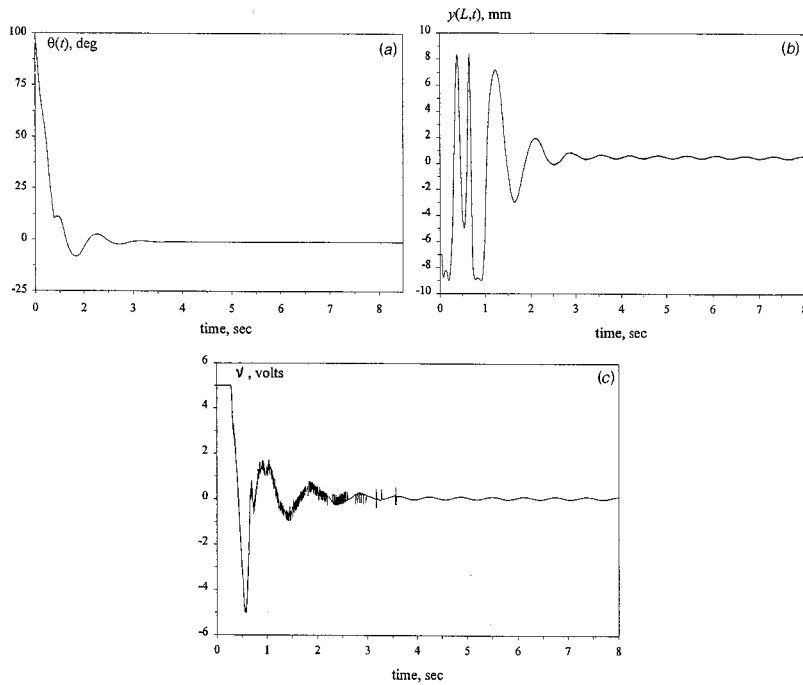
Fig. 5 Experimental system responses to controller with inclusion of arm flexibility, i.e., $\mu = -0.66$; (a) arm angular position, (b) arm tip deflection, and (c) control voltage applied to DC servomotor

This, in turn, demonstrates the capability of the proposed control scheme when considerable deviations between model and plant are encountered. The only noticeable difference is fast decaying response as shown in Figs. 5(b) and 5(c). This clearly indicates the high friction at the motor, which was not considered in the simulations (Figs. 2(b) and 2(c)).

Similar responses are obtained when the controller is designed based on the rigid-link only, i.e., $\mu = 0$. The system responses are displayed in Fig. 6. Similarly, the undesirable arm tip oscillations are obvious. The overall agreement between simulations (Figs. 2 and 3) and that of experiment (Figs. 5 and 6) is one of the critical contributions if this work.

Fig. 6 Experimental system responses to controller without inclusion of arm flexibility, i.e., $\mu = 0$; (a) arm angular position, (b) arm tip deflection, and (c) control voltage applied to DC servomotor

7 Conclusions

An exponentially stable variable structure controller has been applied to regulation of the angular displacement of a lightweight one-link flexible robot arm. The governing equations with the corresponding boundary conditions have been derived, and the controller was designed based on the original distributed system. An additional on-line perturbation estimation has been introduced and integrated with the control routine to overcome the effect of unmodeled dynamics and measurement imperfections. Numerical simulations along with experimental validations have been provided to demonstrate the superior features of the controller. Utilizing only the arm base angular position and tip deflection in the experiment, it has been shown that the proposed technique is capable of tracking arm while simultaneously suppressing transient vibration at the arm.

Acknowledgment

The author would like to thank Associate Editor Prof. Christopher Rahn, and the reviewers for their comments and careful review that have improved the quality of the paper.

References

[1] Sinha, A., 1988, "Optimum Vibration Control of Flexible Structures for Specified Modal Decay Rates," J. Sound Vib., **123**, No. 1, pp. 185–188.
[2] Skaar, S. B., and Tucker, D., 1986, "Point Control of a One-link Flexible Manipulator," ASME J. Appl. Mech., **53**, pp. 23–27.
[3] Bayo, E., 1987, "A Finite-Element Approach to Control the End-point Motion of a Single-link Flexible Robot," J. Rob. Syst., **4**, pp. 63–75.
[4] Ge, S. S., Lee, T. H., and Zhu, G., 1997, "A Nonlinear Feedback Controller for a Single-link Flexible Manipulator Based on a Finite Element Method," J. Rob. Syst., **14**, No. 3, pp. 165–178.
[5] Yuh, J., 1987, "Application of Discrete-time Model Reference Adaptive Control to a Flexible Single-link Robot," J. Rob. Syst., **4**, pp. 621–630.
[6] de Querioz, M. S., Dawson, D. M., Agrawal, M., and Zhang, F., 1999, "Adaptive Nonlinear Boundary Control of a Flexible Link Robot Arm," IEEE Trans. Rob. Autom., **15**, No. 4, pp. 779–787.
[7] Chalhoub, N. G., and Ulsoy, A. G., 1987, "Control of Flexible Robot Arm: Experimental and Theoretical Results," ASME J. Dyn. Syst., Meas., Control, **109**, pp. 299–309.
[8] de Querioz, M. S., Dawson, D. M., Nagarkatti, S. P., and Zhang, F., 2000, *Lyapunov-Based Control of Mechanical Systems*, Birkhauser Boston.
[9] Lou, Z. H., 1993, "Direct Strain Feedback Control of Flexible Robot Arms: New Theoretical and Experimental Results," IEEE Trans. Autom. Control, **38**, No. 11, pp. 1610–1622.
[10] Yeung, K. S., and Chen, Y. P., 1989, "Regulation of a One-link Flexible Robot Arm using Sliding Mode Control Technique," Int. J. Control, **49**, No. 6, pp. 1965–1978.
[11] Singh, T., Golnaraghi, M. F., and Dubly, R. N., 1994, "Sliding-Mode/Shaped-Input Control of Flexible/Rigid Link Robots," J. Sound Vib., **171**, No. 2, pp. 185–200.
[12] Jalili, N., Elmali, H., Moura, J., and Olgac, N., 1997, "Tracking Control of a Rotating Flexible Beam Using Frequency-Shaped Sliding Mode Control," *Proceedings of the 16th American Control Conference*, pp. 2552–2556, Albuquerque, NM.
[13] Bontsema, J., Cartain, R. F., and Schumacher, J. M., 1988, "Robust Control of Flexible Systems: A Case Study," Automatica, **24**, pp. 177–186.
[14] Zhu, G., Ge, S. S., and Lee, T. H., 1997, "Variable Structure Regulation of a Flexible Arm with Translational Base," *Proceedings of 36th IEEE Conference on Decision and Control*, pp. 1361–1366, San Diego, CA.
[15] Elmali, H., and Olgac, N., 1992, "Sliding Mode Control with Perturbation Estimation (SMCPE): A New Approach," Int. J. Control, **56**, No. 1, pp. 923–941.
[16] Jalili, N., and Olgac, N., 1998, "Time-Optimal/Sliding Mode Control Implementation for Robust Tracking of Uncertain Flexible Structures," Mechatronics, **8**, No. 2, pp. 121–142.
[17] Luo, Z. H., Guo, B. Z., and Morgul, O., 1999, *Stability and Stabilization of Finite Dimensional Systems with Applications*, Springer-Verlag, London.
[18] Junkins, J. L., and Kim, Y., 1993, *Introduction to Dynamics and Control of Flexible Structures*, Washington, DC; AIAA Educational Series.
[19] Yeung, K. S., and Chen, Y. P., 1988, "A New Controller Design for Manipulators using the Theory of Variable Structure Systems," IEEE Trans. Autom. Control, **33**, pp. 200–206.
[20] Slotine, J. J., and Li, W., 1991, *Applied Nonlinear Control*, Prentice-Hall, NJ.
[21] Moura, J. T., Roy, R. G., and Olgac, N., 1997, "Frequency-Shaped Sliding Modes: Analysis and Experiments," IEEE Trans. Control Syst. Technol. **5**, No. 4, pp. 394–401.
[22] Slotine, J. J., and Sastry, S. S., 1983, "Tracking Control of Non-linear Systems using Sliding Surface with Application to Robot Manipulators," Int. J. Control, **38**, No. 2, pp. 465–492.
[23] MAPLE, Waterloo Maple Inc, Ontario Canada © 2000.
[24] Cannon, Jr., R. H., and Schmitz, E., 1984, "Initial Experiments on the end-point Control of a Flexible One-link Robot," Int. J. Robot. Res., **3**, No. 3, pp. 62–75.
[25] Feliu, V., Rattan, K. S., and Brown, Jr., H., 1990, "Adaptive Control of a Single-link Flexible Manipulator," IEEE Control Syst. Mag., **10**, pp. 29–33.

A Note on the Computation of the Euler Parameters

Lars Johansson

Division of Mechanics, Department of Mechanical Engineering, Linköping University, SE-581 83 Linköping, Sweden
e-mail: largo@ikp.liu.se

This paper is concerned with the integration of the differential equations for the Euler parameters, for the purpose of describing the orientation of a rigid body. This can be done using standard methods, but in some cases, such as in the presence of impulsive forces, the angular velocities are not continuous and methods based on high order continuity are not appropriate. In this paper, the use of the closed-form solution for piecewise constant angular velocity as the basis for a computational algorithm is studied. It is seen that if this solution is implemented in a leapfrog manner a method with second-order accuracy is obtained in the smooth case, while this method also makes sense in the discontinuous case. [DOI: 10.1115/1.1408943]

1 Introduction

The orientation of a rigid body is determined by integrating the differential equations for one of the several sets of parameters available to describe its orientation. One such set of orientation parameters are the Euler parameters, which are related to $\boldsymbol{\omega}$ by (Wittenburg [1]):

$$\frac{d\mathbf{q}}{dt} = \mathbf{Q}(t)\mathbf{q} = -\frac{1}{2}\begin{bmatrix} 0 & \omega_x & \omega_y & \omega_z \\ -\omega_x & 0 & -\omega_z & \omega_y \\ -\omega_y & \omega_z & 0 & -\omega_x \\ -\omega_z & -\omega_y & \omega_x & 0 \end{bmatrix}\begin{bmatrix} q_0 \\ q_1 \\ q_2 \\ q_3 \end{bmatrix} \quad (1)$$

Here ω_x, ω_y, and ω_z are the components in body fixed coordinates xyz of the angular velocity vector $\boldsymbol{\omega}$ and the Euler parameters are defined as

$$q_0 = \cos(\alpha/2)$$

$$q_1 = n_x \sin(\alpha/2)$$

$$q_2 = n_y \sin(\alpha/2)$$

$$q_3 = n_z \sin(\alpha/2)$$

where α is the angle that the body must rotate about the direction $\mathbf{n} = [n_x, n_y, n_z]^t$ to reach its current position from the reference configuration. The Euler parameters satisfy the following normalization condition:

$$q_0^2 + q_1^2 + q_2^2 + q_3^2 = 1 \quad (2)$$

The present paper is concerned with the calculation of the Euler parameters from (1), assuming that the angular velocity is known with sufficient accuracy at one or several previous time instances, from numerical solution of the rotational equations of motion or otherwise. A straightforward approach is to solve the differential equation (1) for the Euler parameters numerically by some established method of high accuracy such as Runge-Kutta, typically fourth order, or Adams-Bashforth, typically third order. In the derivation of these methods it is assumed that the sought function is several times continuously differentiable. However, in cases with impulsive forces, such as rigid body frictional impact, the angular velocity is discontinuous, resulting in a discontinuous first derivative of the Euler parameters and thus removing the basis of these methods. In, for example, Johansson and Klarbring [2] and Johansson [3,4] problems of this type are studied.

The closed-form solution for the Euler parameters for a constant angular velocity has been used to calculate the Euler parameters, assuming a piecewise constant angular velocity, Whitmore et al. [5] although this does not seem to be common; some authors feel that this approach is not accurate enough, e.g., Stevens and Lewis [6]. An obvious idea would be to calculate solutions assuming higher order variations of the angular velocity. However, while solutions are available for more general variations of the angular velocity, these are unattractively complicated, see Morton et al. [7].

In the present paper, the case where a piecewise constant assumption for the angular velocity is implemented in a leapfrog type algorithm is studied. Thus, the angular velocity is assumed to be available at the midpoints between the points where the Euler parameters are computed. Sections 2 and 3 are concerned with the properties of this method when the angular velocities are smooth, i.e., between impacts, so that it can be assumed that the Euler parameters are smooth. It is seen that the approximation is better than might be expected from the piecewise constant assumption; if the angular velocity has constant direction the proposed method corresponds to assuming a piecewise linear variation of its magnitude while in the case when the angular velocity does not have constant direction, the proposed method will still work as a globally second-order accurate computation method for the Euler parameters. This last point can be considered the main point of the present paper. Finally, in Section 4, numerical examples are given where the present method is compared to other methods when applied to discontinuous angular velocities.

2 The Constant Angular Velocity Solution

If $\mathbf{Q}$ is constant and the Euler parameters are known at some time, say $t = t_0$, the solution to (1) can be written in closed form as

$$\mathbf{q}(t) = e^{\mathbf{Q} \cdot (t - t_0)} \mathbf{q}(t_0) \tag{3}$$

An approximate method for time varying $\mathbf{Q}$ is obtained by choosing T as a time interval, short compared to the total time interval of interest, and assuming that $\mathbf{Q}(t)$ is constant at its value at the midpoint of the interval. The Euler parameters at time $t = T/2$ can then be computed as

$$\mathbf{q}_{1/2} = e^{\mathbf{Q}_0 T} \mathbf{q}_{-1/2}, \tag{4}$$

and the process is repeated to cover the desired time interval, giving a leapfrog type computational scheme based on approximating the angular velocity as piecewise constant. Since this scheme is based on the closed-form solution for a special case, the normalization condition (2) will be satisfied exactly (within the limits of computer accuracy). Here and elsewhere in this paper a subscript will denote the value of a quantity at a certain time so that $\mathbf{q}_{-1/2} = \mathbf{q}(-T/2)$ etc. Equation (4) will be called the uncorrected 1-point formula. It will be seen below that this equation also gives the exact solution for a the case of an angular velocity

with piecewise linearly varying magnitude but constant direction. The case of an angular velocity with changing direction will be treated in Section 3.

Due to the special structure of $\mathbf{Q}$ the matrix exponential in (4) can be calculated from, c.f. Whitmore et al. [5]:

$$e^{\mathbf{Q}T} = \mathbf{1} \cos\left(\frac{T}{2}|\boldsymbol{\omega}|\right) + \frac{2\mathbf{Q}}{|\boldsymbol{\omega}|} \sin\left(\frac{T}{2}|\boldsymbol{\omega}|\right) \tag{5}$$

where $|\boldsymbol{\omega}| = \sqrt{\omega_x^2 + \omega_x^2 + \omega_x^2}$ is the length of the vector from which $\mathbf{Q}$ is constructed, c.f. Eq. (1), and $\mathbf{1}$ is the unit matrix. It is tempting to try to derive more accurate schemes by assuming that $\mathbf{Q}$ is a piecewise linear function of time, or piecewise quadratic etc. Unfortunately, the closed-form solution (3) to (1) cannot be generalized in a straightforward manner, since

$$\mathbf{q}(t) = e^{\int_{t_0}^t \mathbf{Q}(s)ds} \mathbf{q}(t_0) \tag{6}$$

is not in general a solution to (1). It is a solution to (1) if $\mathbf{Q}(t)$ has the commutative property:

$$\mathbf{Q}(t) \int_{t_0}^t \mathbf{Q}(s)ds = \int_{t_0}^t \mathbf{Q}(s)ds\, \mathbf{Q}(t) \tag{7}$$

see Lukes [8], where a slightly more general case is treated, and Byers and Vadali [9]. This condition is fulfilled if the angular velocity from which $\mathbf{Q}(t)$ is constructed has constant direction, c.f. Section 3. It then holds that

$$\frac{d}{dt} e^{\int_{t_0}^t \mathbf{Q}(s)ds} = \mathbf{Q}(t) e^{\int_{t_0}^t \mathbf{Q}(s)ds}. \tag{8}$$

Accepting the (rather strong) assumption of (7) we note that (4) will also be exact for a piecewise linear variation of $\boldsymbol{\omega}$ since the midpoint rule of integration

$$\int_{-T/2}^{T/2} \mathbf{Q}(t)dt = \mathbf{Q}_0 \cdot (T + \mathcal{O}(T^3))$$

is exact for a linear variation of $\mathbf{Q}(t)$, c.f. Dahlquist et al. [10], so that (4) is then recovered from (6). This result is given, in a slightly different context, by Byers and Vadali [9]. It is thus seen that for the case of constant direction $\boldsymbol{\omega}$, the scheme based on (4) amounts to approximating $\boldsymbol{\omega}$ as piecewise linear and compute the closed form solution to this approximation. Cases where $\boldsymbol{\omega}$ has constant direction and piecewise linear direction with jumps could also be computed exactly (within the limits of computer accuracy) in this way if the jumps are situated precisely at the points where the Euler parameters are evaluated.

3 The Non-Commutative Case

In this section the behavior of the algorithm based on Eq. (4) will be studied for the case when the angular velocity is smooth but otherwise general i.e., Eq. (7) is not satisfied. It will be seen that a globally second-order accurate numerical scheme is obtained for this case.

To develop a correction for the case when $\boldsymbol{\omega}(t)$ is allowed to change direction as well as magnitude, $\mathbf{Q}(t)$ is written

$$\mathbf{Q}(t) = \mathbf{Q}^{\|}(t) + \mathbf{Q}^{\perp}(t)$$

where $\mathbf{Q}^{\|}(t)$ satisfies (7) and $\mathbf{Q}^{\perp}(t)$ does not. Such a decomposition can be constructed by selecting a constant direction $\mathbf{n}$ and writing the angular velocity from which $\mathbf{Q}(t)$ is constructed as

$$\boldsymbol{\omega}(t) = (\boldsymbol{\omega} \cdot \mathbf{n})\mathbf{n} + (\boldsymbol{\omega} - (\boldsymbol{\omega} \cdot \mathbf{n})\mathbf{n}) = f(t)\mathbf{n} + (\boldsymbol{\omega} - f(t)\mathbf{n}) = \boldsymbol{\omega}^{\|} + \boldsymbol{\omega}^{\perp}. \tag{9}$$

If $\mathbf{Q}^{\|}(t)$ is taken to be the part of $\mathbf{Q}(t)$ corresponding to $\boldsymbol{\omega}^{\|} = f(t)\mathbf{n}$, it is a scalar function of time multiplied by a constant matrix, which will satisfy (7).

Using this decomposition, (1) can be written

$$\dot{\mathbf{q}} = \mathbf{Q}(t)\mathbf{q} = (\mathbf{Q}^{\|}(t) + \mathbf{Q}^{\perp}(t))\mathbf{q}. \tag{10}$$

Next, the solution is assumed to be of the form

$$\mathbf{q}(t) = e^{\int_{t_0}^{t} \mathbf{Q}^{\parallel}(s)ds} \mathbf{q}(t_0) + \mathbf{q}^{\perp}(t) \tag{11}$$

with

$$\mathbf{q}^{\perp}(t_0) = \mathbf{0}. \tag{12}$$

Inserting (11) into (10) gives, using (8),

$$\dot{\mathbf{q}}^{\perp} = \mathbf{Q}^{\perp} e^{\int_{t_0}^{t} \mathbf{Q}^{\parallel}(s)ds} \mathbf{q}(t_0) + \mathbf{Q}\mathbf{q}^{\perp}. \tag{13}$$

Setting $t_0 = -T/2$ and using a central difference and averaging discretization we have from (13):

$$\frac{\mathbf{q}_{1/2}^{\perp} - \mathbf{q}_{-1/2}^{\perp}}{T} = \mathbf{Q}_0^{\perp} e^{\int_{-T/2}^{0} \mathbf{Q}^{\parallel}(s)ds} \mathbf{q}_{-1/2} + \mathbf{Q}_0 \frac{\mathbf{q}_{-1/2}^{\perp} + \mathbf{q}_{1/2}^{\perp}}{2} + \mathcal{O}(T^2). \tag{14}$$

Note that the fourth time derivative of $\mathbf{q}^{\perp}$ is required to exist in this step, Vandergraft [11]

From (14), (11), and (12) we obtain the Euler parameters at time $t = T/2$ as

$$\mathbf{q}_{1/2} = e^{\int_{-T/2}^{T/2} \mathbf{Q}^{\parallel}(s)ds} \mathbf{q}_{-1/2} + \frac{1 + \mathbf{Q}_0 T/2}{1 + |\boldsymbol{\omega}_0|^2 T^2/16} T \mathbf{Q}_0^{\perp} e^{\int_{-T/2}^{0} \mathbf{Q}^{\parallel}(s)ds} \mathbf{q}_{-1/2}$$
$$+ \mathcal{O}(T^3) \tag{15}$$

where the inverse

$$(\mathbf{1} - \mathbf{Q}_0 T/2)^{-1} = \frac{1 + \mathbf{Q}_0 T/2}{1 + |\boldsymbol{\omega}_0|^2 T^2/16},$$

see Omelyan [12], has been used. In Eq. (15) the first term to the right is the exact solution if the angular velocity has constant direction, the second term is a correction if it has not and the third term is the truncation error of the correction.

It is immediately observed that if we put

$$\mathbf{n} = \boldsymbol{\omega}_0 / |\boldsymbol{\omega}_0| \tag{16}$$

that is, if we decide to take the direction of $\boldsymbol{\omega}$ at time $t = 0$ as the direction on which the split of $\boldsymbol{\omega}$ in (9) is based then

$$\mathbf{Q}_0^{\perp} = \mathbf{Q}^{\perp}(t = 0) = \mathbf{0} \tag{17}$$

and (15) becomes

$$\mathbf{q}_{1/2} = e^{\int_{-T/2}^{T/2} \mathbf{Q}^{\parallel}(s)ds} \mathbf{q}_{-1/2} + \mathcal{O}(T^3) \tag{18}$$

The first term to the right of Eq. (18) provides us with a globally second-order accurate scheme for the Euler parameters if it is used repeatedly to cover the time interval of interest (or the exact solution if it so happens that $\mathbf{Q}^{\perp}(t) = \mathbf{0}$).

Next, we turn to the evaluation of the integral in Eq. (18). By the midpoint rule we have, c.f. Dahlquist et al. [10]:

$$\int_{-T/2}^{T/2} \mathbf{Q}^{\parallel}(s)ds = \mathbf{Q}_0^{\parallel} \cdot (T + \mathcal{O}(T^3)) = \mathbf{Q}_0 \cdot (T + \mathcal{O}(T^3)), \tag{19}$$

where (17) has been used.

Inserting (19) into (18) gives

$$\mathbf{q}_{1/2} = e^{\mathbf{Q}_0 \cdot (T + \mathcal{O}(T^3))} \mathbf{q}_{-1/2} + \mathcal{O}(T^3)$$
$$= e^{\mathbf{Q}_0 T} e^{\mathbf{Q}_0 \mathcal{O}(T^3)} \mathbf{q}_{-1/2} + \mathcal{O}(T^3) = e^{\mathbf{Q}_0 T} \mathbf{q}_{-1/2} + \mathcal{O}(T^3) \tag{20}$$

which will be called the corrected 1-point formula. Note that the detailed form of the truncation error $\mathcal{O}(T^3)$ changes in the last equality. The second equality holds because a constant matrix satisfies the commutative property, c.f. Lukes [8].

It is noted that the corrected 1-point formula (20) is the same as the uncorrected 1-point formula (4), apart from the $\mathcal{O}(T^3)$ term. It has thus been established that if the formula for piecewise constant $\mathbf{Q}(t)$ is implemented as a leapfrog method it gives a globally second order accurate solution for a general variation of $\mathbf{Q}(t)$. For

the case when the orientation is described using the components of the transformation matrix rather than the Euler parameters a corresponding result is established by Omelyan [13], using a different line of thought for the derivations.

Keeping (16), Eq. (18) can be used with other numerical integration rules, with the same level of approximation for the part $\mathbf{Q}^{\perp}(t)$ of $\mathbf{Q}(t)$ not fulfilling (7). For example, a corrected 3-point formula based on a piecewise quadratic variation of $\mathbf{Q}(t)$ is

$$\mathbf{q}_{1/2} = e^{1/24(25\mathbf{Q}_0 - 2\mathbf{Q}_{-1}^{\parallel} + \mathbf{Q}_{-2}^{\parallel})T} \mathbf{q}_{-1/2} + \mathcal{O}(T^3)$$

4 Numerical Examples

In this section the 1-point method is tested on some examples with discontinuous angular velocity. The results using fourth-order Runge-Kutta and third-order Adams-Bashforth (see e.g. [10,6,11]) are included for comparison; as expected these latter methods doesn't work well since they cannot be expected to handle the discontinuities well.

Two different angular velocities are used. In both cases ω_x and ω_y are zero, while ω_z varies as shown in Fig. 1. Physically the case with an alternating piecewise constant ω_z might be a bouncing so-called superball, see Vu-Quoc et al. [14], while the increasing piecewise constant ω_z might correspond to a ball bouncing with friction on a surface whose speed is increasing. In both these cases closed form solutions can be computed.

The error to be studied is computed as

$$\text{error} = |\mathbf{q}_{\text{numeric}} - \mathbf{q}_{\text{exact}}| / |\mathbf{q}_{\text{exact}}|.$$

Obviously, for a numerical method to be accurate, this error should be small compared to 1. It can be noted that, because of the normalization condition (2), $|\mathbf{q}_{\text{exact}}| = 1$. If the numerical solution also fulfills this condition, which the 1-point formula does, the error can never be larger than 2. The timesteps used below are 0.051 and 0.0051 seconds. These are selected to avoid putting the discontinuities at an integral number of timesteps, in which case the 1-point method under investigation would give a closed form solution to the examples and the only errors would be related to computer accuracy.

In Fig. 2 the results for a piecewise constant stepwise increasing ω_z is shown for a timestep of 0.051 seconds. It is seen that the 1-point method gives reasonably small errors while the Runge-Kutta and Adams-Bashforth methods manages to follow the solution for a while but then breaks off to unacceptable errors. The Adams-Bashforth solution in fact becomes numerically unstable after a while. Figure 3 shows the results using a smaller timestep to avoid this instability, but the observation that Runge-Kutta and Adams-Bashforth methods eventually breaks of to unacceptable errors still holds true.
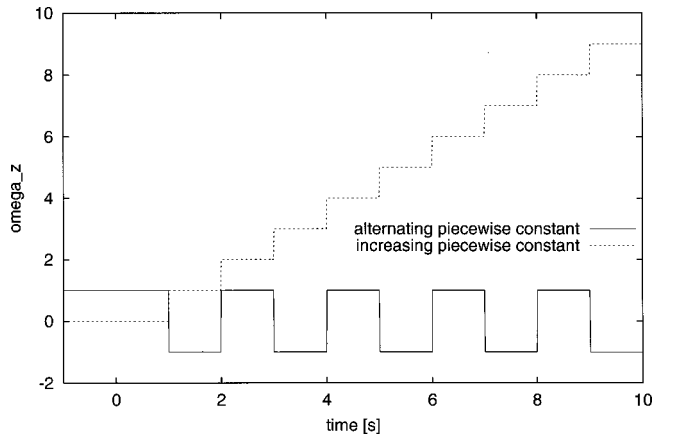

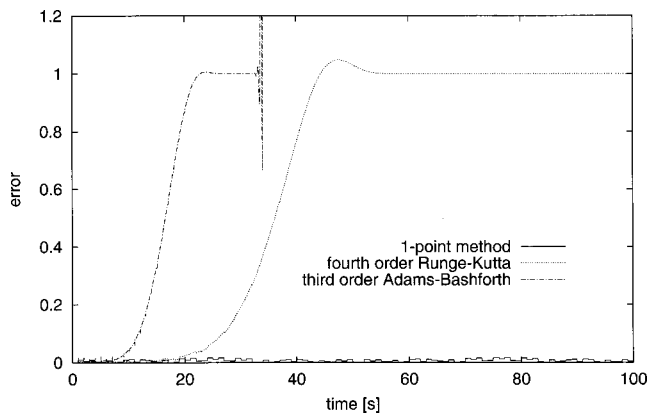Fig. 1 Variation of ω_z in the examples

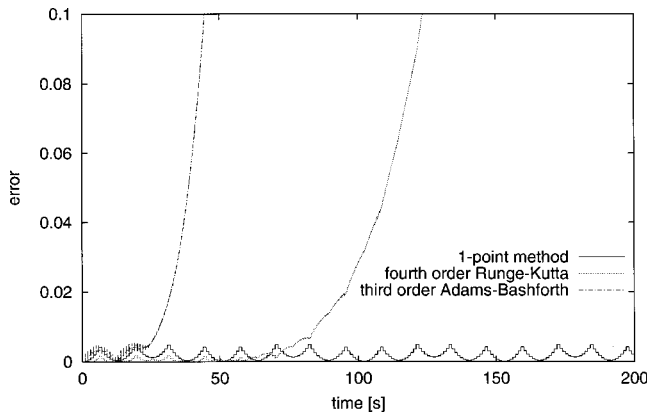**Fig. 2 Errors for increasing piecewise constant ω_z**

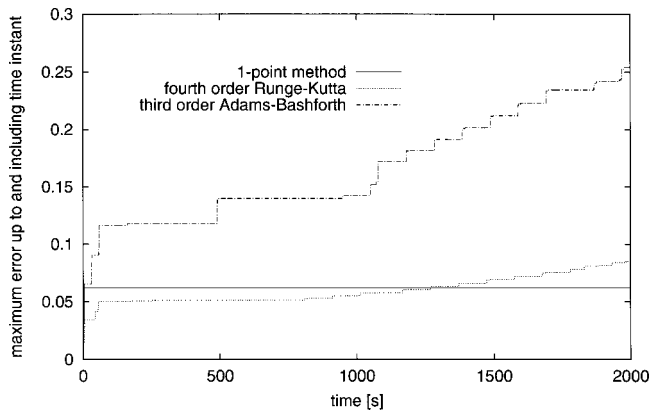**Fig. 3 Errors for increasing piecewise constant ω_z, short timestep**

Fig. 4 Errors for alternating piecewise constant ω_z

In Fig. 4 the results for alternating piecewise constant ω_z are shown. This figure shows the maximum error occurring up to and including a certain time instant rather than the error at each time. Again it is seen that the Runge-Kutta and Adams-Bashforth methods tends to break away to large errors, although the advantage of the 1-point method is not quite as pronounced as in the previous example.

5 Discussion

In this paper the solution of the differential equation for the Euler parameters have been discussed. The closed form solution for piecewise constant angular velocity is attractive for motion with discontinuous angular velocity, but a more accurate method is desirable if such motion is combined with long intervals of motion with smoothly varying angular velocity.

Unfortunately, there are no simple closed-form solutions for higher order variation of the angular velocity, unless the direction is constant. This paper is therefore concerned with the implementation of the piecewise constant solution in a leapfrog type algorithm. This method works well for discontinuous angular velocities, as indicated by the numerical examples, and provides a second order accurate algorithm for cases with smooth but otherwise general variation of the angular velocity. The method is also exact for cases of constant angular velocity and constant direction angular velocity with linearly varying magnitude, which makes it attractive for spinning objects such as flywheels. In conclusion, the proposed method should be appropriate for problems with large numbers of impacts, such as that studied in Johansson [4] or problems with occasional impacts and periods of free flight with high angular velocity with constant direction, such as in Johansson [3].

References

[1] Wittenburg, J., 1977, *Dynamics of Systems of Rigid Bodies*, Teubner, Stuttgart.
[2] Johansson, L., and Klarbring, A., 2000, "Study of Frictional Impact Using a Non-Smooth Equations Solver," ASME J. Appl. Mech., **67**, pp. 267–273.
[3] Johansson, L., 1999, "A Linear Complementarity Algorithm for Rigid Body Impact with Friction," European Journal of Mechanics, **18**, pp. 703–717.
[4] Johansson, L., "A Newton Method for Rigid Body Frictional Impact with Multiple Simultaneous Impact Points," Comput. Methods Appl. Mech. Eng., to appear.
[5] Whitmore, S. A., Fife, M., and Logan, B., 1997, "Development of a Closed-Loop Strap Down Attitude System for an Ultralight Altitude Flight Experiment," NASA Technical Memorandum 4775.
[6] Stevens, B. L., and Lewis, F. L., 1992, *Aircraft Control and Simulation*, Wiley, New York.
[7] Morton, H. S., Junkins, J. L., and Blanton, J. N., 1974, "Analytical Solutions for Euler Parameters," Celest. Mech., **10**, pp. 287–301.
[8] Lukes, D. H., 1982, *Differential Equations: Classical to Controlled*, Academic Press, New York.
[9] Byers, R. M., and Vadali, S. R., 1993, "Qasi-Closed-Form Solution to the Time-Optimal Rigid Spacecraft Reorientation Problem," J. Guid. Control Dyn., **16**, pp. 453–461.
[10] Dahlquist, G, Björk, A, and Anderson, N., 1974, *Numerical Methods*, Prentice-Hall, Englewood Cliffs.
[11] Vandergraft, J. S., 1978, *Introduction to Numerical Computations*, Academic Press, New York.
[12] Omelyan, I. P., 1998, "Algorithm for Numerical Integration of the Rigid-Body Equations of Motion," Phys. Rev. E, **58**, pp. 1169–1172.
[13] Omelyan, I. P., 1998, "Numerical Integration of the Equations of Motion for Rigid Polyatomics: The Matrix Method," Comput. Phys. Commun., **109**, pp. 171–183.
[14] Vu-Quoc, L., Zhang, X., and Walton, O. R., 2000, "A 3-D Discrete-Element Method for Dry Granular Flows of Ellipsoidal Particles," Comput. Methods Appl. Mech. Eng., **187**, pp. 483–528.

A Switching Scheme for Mixed PZT-Based/Jet Thrusters Control of a Large Flexible Structure

A. Ferrara, L. Magnani, and R. Scattolini
Dipartimento di Informatica e Sistemistica,
Via Ferrata 1, 27100 Pavia, Italy
e-mail: antonella.ferrara@unipv.it

Vibration suppression of a large space structure is achieved by switching between different actuators in order to optimize control performance and to reduce energy consumption. The theoretical properties of the proposed control strategy are reported together with some experimental results. [DOI: 10.1115/1.1408609]

1 Introduction

On/off jet thrusters have often been used for vibration suppression in large flexible space structures, see e.g., [1,2] where empirical control switching strategies have been adopted or [3,4] where the Variable Structure Control (VSC) technique has been applied. When a bang-bang control action is not sufficient, piezoelectric rods can be used as both structural and actuation elements, see e.g., [5,6]. An interesting technological solution can include both jet thrusters for the suppression of large vibrations and piezoelectric actuators for the damping of residual vibrations. This configuration has been considered here for the control of the large flexible experimental space structure shown in Fig. 1.

The space structure is located at the Department of Aerospace Engineering at the Politecnico di Milano and has been already considered in [2,4,7]. It is a modular truss with mass of 75 Kg, length of 19 m, built with commercial PVC elements for a total of 54 cubic bays. The truss is suspended by three pairs of steel springs ensuring a satisfactory decoupling of rigid and elastic bending modes. It has been designed so that the bending modes in the horizontal and in the vertical plane are independent, although closely spaced in frequency. Hence, the controller can be designed and implemented in the horizontal plane only.

The truss is equipped with six pairs of on-off air jet thrusters, each one delivering a non-modulable force of about 2.1 N when supplied with air at 3 bar. Thrust is generated with a delay of about 12 ms after the transmission of the control command, and the actuators do not operate properly at switching frequencies greater than 40 Hz. The structure includes also six active piezoelectric rods substituting symmetric passive PVC elements and providing a maximum traction force of 700 N and a maximum compression force of 3000 N, with input voltage range [0 V, 100 V]. Standard amplifiers provide high bandwidth gain and bias the piezoelectric actuators at their midpoint. The rods also exhibit an hysteresis which has been considered in the simulation model, but which has not been included into the linear model used in the preliminary control synthesis phase. The horizontal motion of the truss is measured by six accelerometers, whose outputs are processed by analog and digital filters, so that only the first eight natural modes in the horizontal plane can be considered in the control problem. These filters introduce a phase lag equivalent to a delay of about 60 ms at the sampling frequency of 200 Hz.

2 Mathematical Model

Let η be the vector of the amplitudes of the vibration modes, u_J and u_P be the control variables associated with the jets and the piezoelectric actuators, respectively, y be the vector of acceleration measurements. Moreover, denote by Φ the matrix of the modal shape vectors, by Ω and Ξ the matrices of natural frequen-
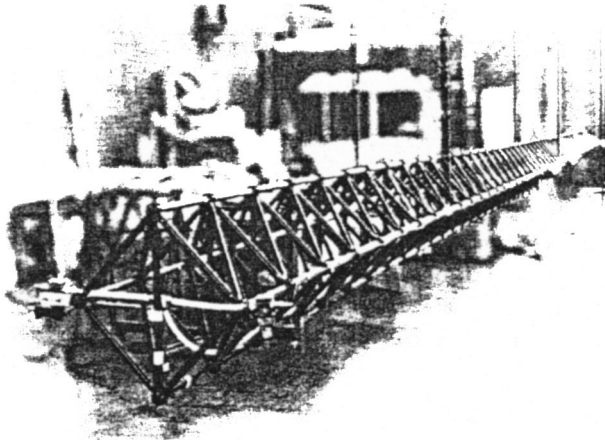

Fig. 1 The experimental device

Table 1 Natural frequencies and damping coefficients

Mode	ω_n [Hz]	ξ	Mode	ω_n [Hz]	ξ
rigid rotation	0.2823	0.0032	III bending	5.4506	0.0103
rigid translation	0.2870	0.0085	IV bending	8.9540	0.0105
I bending	1.0356	0.0077	V bending	13.0443	0.0100
II bending	2.9185	0.0094	VI bending	17.7674	0.0100

cies and damping coefficients and by I the identity matrix of appropriate size. Neglecting the nonlinearities mainly due to the actuators, the linear mathematical model of the structure is (see [7])

$$\begin{cases} \dot{x}(t) = Ax(t) + B_J u_J(t) + B_P u_P(t) \\ y(t) = Cx(t) + D_J u_J(t) + D_P u_P(t) \end{cases} \quad (1)$$

where $x = [\eta' \ \dot{\eta}']' \in R^{1320}$, $u_J \in R^6$, $u_P \in R^6$, $y \in R^6$ and

$$A = \begin{bmatrix} 0 & I \\ -\Omega^2 & -2\Xi\Omega \end{bmatrix}, \quad B_J = \begin{bmatrix} 0 \\ -\Phi' M_{aJ} \end{bmatrix}, \quad B_P = \begin{bmatrix} 0 \\ -\Phi' M_{aP} \end{bmatrix} \quad (2)$$

$$C = [-M_s\Phi\Omega^2 \ -2M_s\Phi\Xi\Omega], \quad D_J = M_s\Phi\Phi' M_{aJ},$$

$$D_P = M_s\Phi\Phi' M_{aP}$$

In (2) M_s transforms x into the vector of sensor displacements and M_{aJ}, M_{aP} represent the influence of u_J, u_P on the structure.

For simulation and control design purposes, it is advisable to neglect high frequency modes. Hence, a model with 54 state variables suitable for preliminary simulation studies has been derived. Then this model has been further reduced to obtain a model with 16 state variables, which has been used in the control synthesis phase. The natural frequencies ω_n and the damping coefficients ξ of the corresponding eight modes are reported in Table 1.

3 Switching Control Design

Two different VSC control laws, namely VSC_J and VSC_P, for the jet thrusters and for the piezoelectric rods have been designed assuming that one type of actuator is inactive when the other one is used, that is by alternatively setting $u_P = 0$ and $u_J = 0$. In both cases, adjacent and symmetric pairs of actuators have been controlled jointly, so avoiding their simultaneous switching in opposite directions. This introduces a functional dependence between the elements of u_J and u_P, so that only three control variables have to be independently chosen in both cases and reduced input vectors $\bar{u}_J \in R^3$ and $\bar{u}_P \in R^3$ must be considered.

According to [8], the sliding surfaces $\sigma_J(x) = 0$, $\sigma_P(x) = 0$ have been computed by minimizing the cost function

$$J = \frac{1}{2} \int_0^\infty x'(t) Q x(t) dt \quad (3)$$

The elements of the diagonal matrices $Q = Q_J$ and $Q = Q_P$ have been chosen by extensive simulation experiments. Then, the following control laws have been determined:

$$\text{VSC}_J = \begin{cases} \bar{u}_J(t) = -K_J sign(\sigma_J(x)) \\ \bar{u}_P(t) = 0 \end{cases},$$

$$\text{VSC}_P = \begin{cases} \bar{u}_J(t) = 0 \\ \bar{u}_P(t) = -K_P sign(\sigma_P(x)) \end{cases} \quad (4)$$

where the gains K_J and K_P depend on the maximum force delivered by the actuators.

Concerning the control laws 4, the following assumption is in order.

Assumption A1: For the control laws VSC_J and VSC_P there exist closed sets X_J and X_P containing the origin as interior point such that:

1 for any initial state $x(0) \in X_J$ $(x(0) \in X_P)$ the state trajectory reaches $\sigma_J(x) = 0$ $(\sigma_P(x) = 0)$ in a finite time upper-bounded by t_J (t_P);

2 for any $x(0) \in X_J \cap \sigma_J(x) = 0$ $(x(0) \in X_P \cap \sigma_P(x) = 0)$ and any $t \geq 0$, there exist positive constants a and b such that

$$\|x(t)\| \leq a e^{-bt} \|x(0)\| \tag{5}$$

Remark 1. The previous assumption is readily verified in the context of VSC, see [9], *where a proper control law design can guarantee both a finite time reaching of the sliding surface and the exponential stability on it.*

The adopted switching control strategy consists of using the jets for damping both rigid and elastic modes when an "energy function" $E(x) = x' P_c x$, $P_c = \text{diag}\{\Omega^2, I\}$ of the truss is beyond a prescribed threshold C, that is when $x \in X_c = \{x : E(x) > C\}$, while commuting to the piezoelectric rods for the elimination of residual elastic vibrations when $E(x) \leq C$. A priori, this strategy leads to a switched system whose stability properties cannot be guaranteed. For this reason, it is advisable to define a "dwelling time" τ as the time which must be elapsed from the last control switching before a new switching can occur, see [10].

Theorem 1. Assume that: (i) A1 holds; (ii) $X_J \supset X_c$ and $X_P \supset X_c$. Then there exist a computable constant $\bar{C}$ and a computable dwelling time $\bar{\tau}$ such that for any $C > \bar{C}$ and any $\tau > \bar{\tau}$ the switching control strategy makes the origin an asymptotically stable equilibrium point with region of attraction X_J.

Proof: Define $t = \max(t_J, t_P)$ and let $\tau = \bar{t} + \bar{\tau}$, where $\bar{\tau} > 0$ is the minimum time which must be spent on $\sigma_J(x) = 0$ or $\sigma_P(x) = 0$ even if the system state has moved outside the region where the corresponding control law should be used. Note that there exists a positive constant γ such that $\|e^{At}\| \leq \gamma, \forall t \leq \bar{t}$, and a positive constant h such that

$$\int_0^t e^{A\eta} B_J \tilde{K}_J d\eta \leq h, \quad \int_0^t e^{A\eta} B_P \tilde{K}_P d\eta \leq h, \quad \forall t \leq \bar{t}$$

where $\tilde{K}_J$ and $\tilde{K}_P$ are two vectors with the dimensions of K_J and K_P and whose elements have the same absolute value of the corresponding ones of K_J and K_P with any combination of sign.

Now assume that $x(0) \in X_J$ and $x(0) \notin \sigma_J(x) = 0$. Then VSC_J is used and, at a time $t_1 \leq \bar{t}$,

$$\|x(t_1)\| \leq \gamma \|x(0)\| + h$$

with $x(t_1) \in \sigma_J(x) = 0$. Until time $t_2 = t_1 + \bar{\tau}$ the state trajectory is on $\sigma_J(x)$ and

$$\|x(t_2)\| \leq a e^{-b\bar{\tau}} \|x(t_1)\| \leq \gamma a e^{-b\bar{\tau}} \|x(0)\| + a e^{-b\bar{\tau}} h$$

At $t = t_2$, the control law commutes to VSC_P provided that $x(t_2) \in X_P$. Following the same arguments and assuming that there are n commutations between VSC_J and VSC_P, it is possible to verify that

$$\|x(t_{2n+1})\| \leq (\gamma a e^{-b\bar{\tau}})^n \gamma \|x(0)\| + \sum_{i=0}^{n} (\gamma a e^{-b\bar{\tau}})^i h$$

Provided that $\bar{\tau} > \log(a\gamma)/b$, the right hand side of this inequality tends, for $n \to \infty$, to $\varphi = h(1 - \gamma a e^{-b\bar{\tau}})^{-1}$. Denoting by $\lambda_{\min}(P_c)$ the minimum eigenvalue of P_c, if $C > \bar{C} = \varphi^2 \lambda_{\min}(P)$, then the state tends to a point on $\sigma_P(x)$ and inside X_P, so that no other commutation occurs. Finally, observe that both $\bar{\tau}$ and $\bar{C}$ can be computed from the problem data by means of the previous expressions. ∎

4 Implementation Issues

The switching control law has been implemented in digital form with a sampling interval of 5 ms. A standard Kalman predictor has been used, see [2]. It predicts the first eight natural modes 15 steps onward (75 ms) so as to reduce the effect of the phase lag due to the adopted anti-aliasing filters.

When using VSC_J, a dead band has been introduced on the sliding surface to reduce chattering phenomena. The amplitudes of the dead zones have been related to the allowed residual movement at the end of the control action, as discussed in [4]. The use of the local dead band is such that the sliding mode on the sliding surface is not ideal, and is usually called a "quasi-sliding mode," see [11]. As for the rods, their static characteristic is of linear-saturated type, not suitable for an on-off control strategy. Then, the VSC_P control law has been implemented by resorting to the concept of "equivalent control," see [8], according to which the VSC action is obtained by passing the computed control variable through a low-pass filter.

Finally, in order to reduce energy consumption, a maximum acceptable amount of residual movement has been determined and all the control actions have been switched off when the truss energy is below a given threshold.
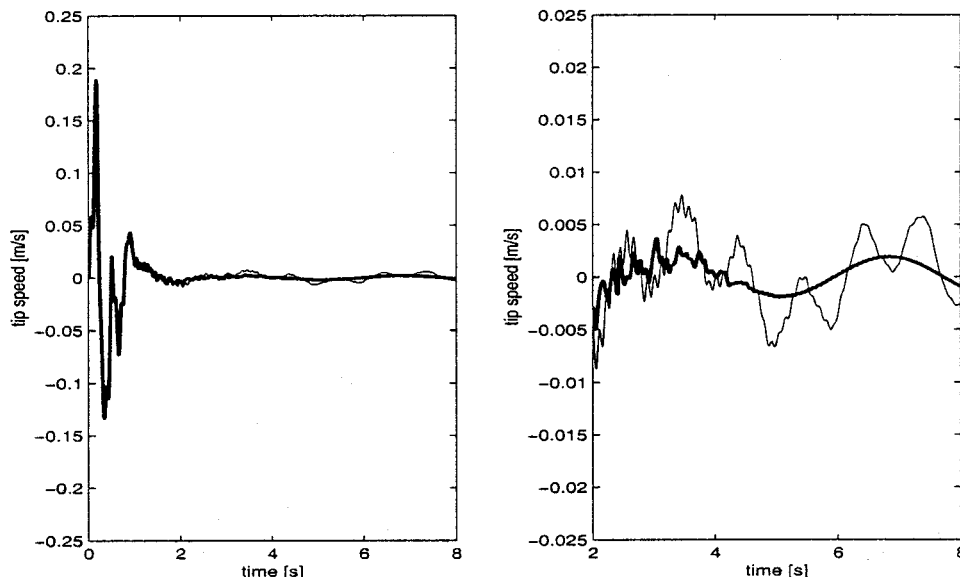

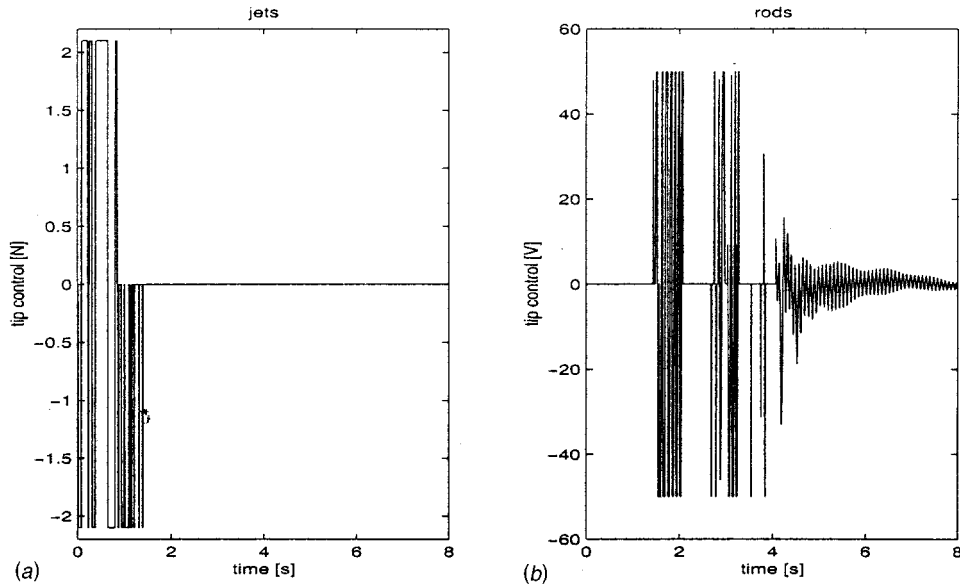**Fig. 2 Tip speed with the switching controller (bold) and with the jets only**

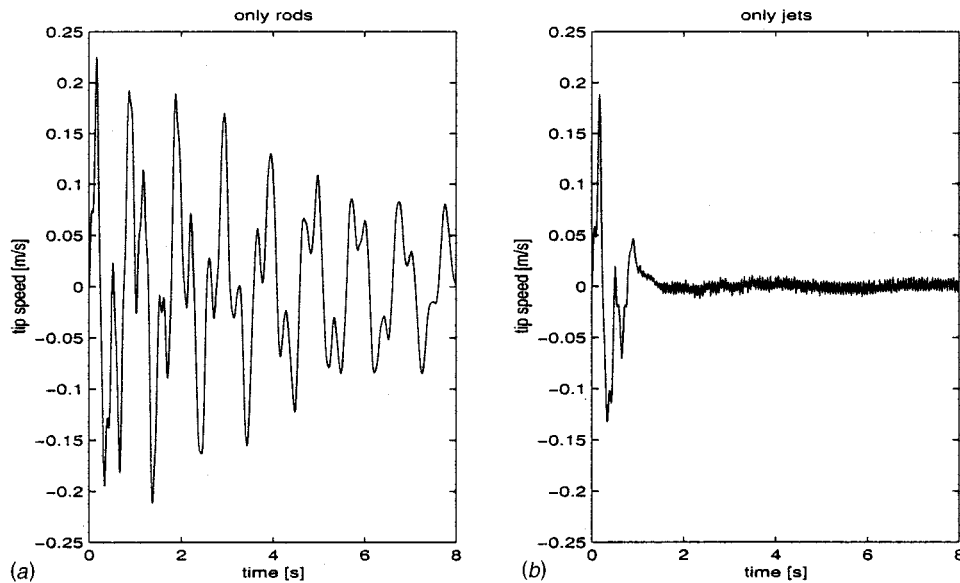**Fig. 3 Control variables: (a) jets, (b) rods**

Fig. 4 Tip speed using (a) only PZT actuators, (b) only jets with a smaller deadzone

5 Simulation and Experimental Results

An extensive preliminary simulation study has been performed to tune the unknown design parameters. The bending modes of interest were excited separately or jointly so as to consider a large number of experimental cases. For brevity, only the results referring to the joint excitation of the four bending modes ($M1 - M4$) at low frequencies are here reported. Specifically, the local velocities at the end of the excitation phase were $v_{M_1} = 0.12$ m/s, $v_{M_2} = 0.12$ m/s, $v_{M_3} = 0.03$ m/s, $v_{M_4} = 0.03$ m/s. Figures 2(a) and 2(b) (which is a zoom of Fig. 2a) compare the transient of the tip speed with VSC$_J$ only to that achieved with the proposed switching strategy. The effect of the rods is evident in the second part of the response, when the jets are switched off and the control action provided by the rods damps the tip oscillations. The corresponding control actions are shown in Fig. 3, where it is apparent that in this case only one transition occurs from the control law VSC$_J$ to VSC$_P$. For comparison, further simulations have been performed

starting from the same initial conditions and using only the rods (control law VSC$_P$) or the jets (control law VSC$_J$ with smaller deadzones) in all the operating range. The corresponding transients are reported in Figs. 4(a) and 4(b), which clearly show that the rods are unable to provide an effective vibration suppression, while an excessive use of the jets causes an useless fuel consumption without any performance improvement.

In all the performed experiments on the real truss, the initial conditions were set using an electromagnetic shaker connected to one end of the structure which brought the truss to a steady oscillation via excitation of one or a combination of its natural frequencies. Then, the shaker was automatically disconnected when the predetermined initial condition was reached. In the results reported here, the excitation of a combination of the first four bending modes was planned in order to mimic as much as possible the previous simulations. Then at the end of the excitation phase, the switching controller was activated. Figures 5(a) and
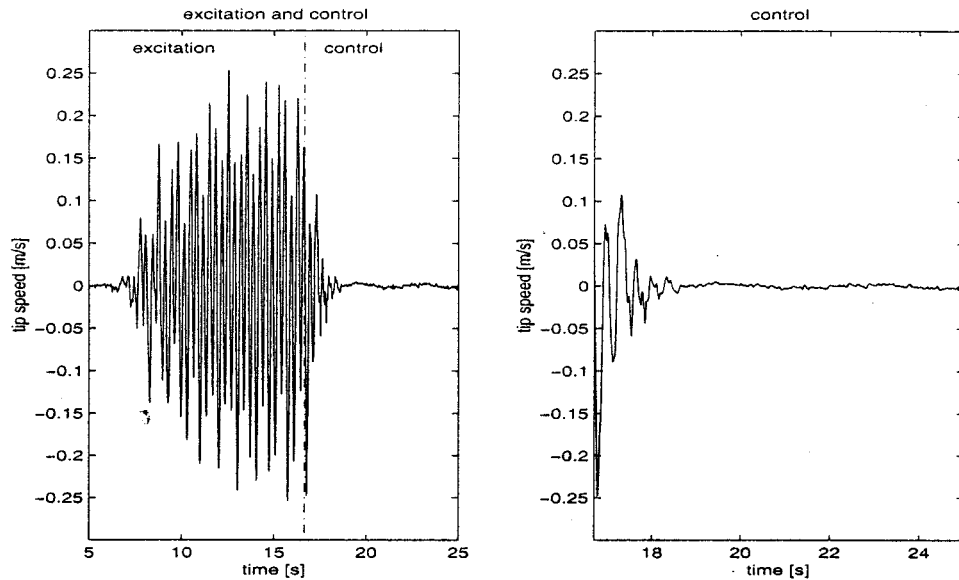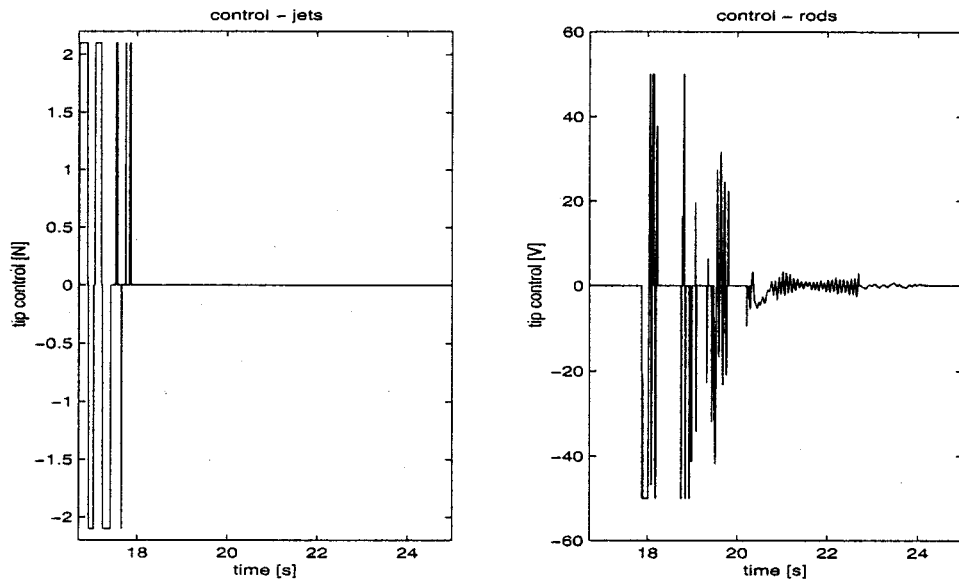
Fig. 5 Tip speed in experimental results

Fig. 6 Control variables in experimental results

5(b)show the experimental tip speed during excitation (t <16.67s) and during the control action (t≥16.67s). The corresponding control variables are reported in Fig. 6. The comparison of Figs. 2 and 5(b)show a good agreement between the simulation and the experimental results. In fact, the 90% settling time is reached after about 1s in simulation and 1.2s in the real experiments. This small discrepancy can be due to an approximate estimation of the damping factors of the bending modes, as well as to the nonlinear dynamics of the actuators.

6 Conclusions

The switching control strategy proposed here for vibration suppression allows to optimize the control performance and to reduce the energy consumption. This is fundamental in space applications, where fuel availability is limited. An extensive experimental phase has witnessed the potentialities of this approach, the theoretical properties of which have also been investigated.

References

[1] Hallauer, W. L., and Lamberson, S., 1989, "Experimental active vibration damping of a plane truss using hybrid actuation," *Proc. of the 30th Structures, Structural Dynamics and Materials Conference*, Mobile, Alabama, pp. 80–90.
[2] Casella, F., Locatelli, A., and Schavoni, N., 1996, "Nonlinear controllers for vibration suppression in a large flexible structure," Control Engineering Practice, **4**, No. 6, pp. 791–806.
[3] Dodds, S. J., and Senior, M., 1993, "A sliding mode approach to the simultaneous shape and attitude control of flexible space structures with uncertain dynamics," *Dynamics and Control of Structures in Space II*, Computational Mechanics Publications, pp. 257–277.
[4] Allen, M., Scattolini, R., and Bernelli-Zazzera, F., 2000, "Sliding mode control of a large flexible structure," Control Engineering Practice, No. 8, pp. 861–871.
[5] Balas, G. J., and Doyle, J. C., 1989, "Robust control of flexible modes in the controller crossover region," *Proc. Amer. Control Conf.*, Pittsburg, PA.

[6] Smith, R. S., Chu, C. C., and Fanson, J. L., 1994, "The design of H_∞ controllers for an experimental non-collocated flexible structure problem," IEEE Trans. Control Syst. Technol., **2**, No. 2, pp. 101–109.

[7] Ercoli-Finzi, A., Gallieni, D., and Ricci, S., 1993, "Design, modal testing and updating of a large space structure Laboratory model," *Proc. of the IXth VPI&SU Symp. on Dynamics and Control of Large Structures*, Blacksburg, VA, pp. 409–420.

[8] Utkin, V. I., 1992, *Sliding Modes in Control Optimization*, Springer-Verlag, Berlin-Heidelberg.

[9] Slotine, J. J., and Li, W., 1991, *Applied Nonlinear Control*, Prentice Hall.

[10] Morse, A. S., 1995, "Control using logic-based switching," *Trends in Control*, A. Isidori, ed., Springer.

[11] Hung, J. Y., Gao, W., and Hung, J. C., 1993, "Variable structure control-a survey," IEEE Trans. Ind. Electron., **40**, No. 1, pp. 2–21.

Intelligent Feedback Linearization for Active Vehicle Suspension Control

Gregory D. Buckner

Assistant Professor, Department of Mechanical and Aerospace Engineering, North Carolina State University, Raleigh, NC 27695

Karl T. Schuetze

Ph.D. Candidate, Department of Mechanical Engineering, The University of Texas at Austin, Austin, TX 78759

Joe H. Beno

Electric Vehicle Program Director, The University of Texas at Austin Center for Electromechanics, Austin, TX 78759

Effective control of ride quality and handling performance are challenges for active vehicle suspension systems, particularly for off-road applications. Off-road vehicles experience large suspension displacements, where the nonlinear kinematics and damping characteristics of suspension elements are significant. These nonlinearities tend to degrade the performance of active suspension systems, introducing harshness to the ride quality and reducing off-road mobility. Typical control strategies rely on linear, time-invariant models of the suspension dynamics. While these models are convenient, nominally accurate, and tractable due to the abundance of linear control techniques, they neglect the nonlinearities and time-varying dynamics present in real suspension systems. One approach to improving the effectiveness of active vehicle suspension systems, while preserving the benefits of linear control techniques, is to identify and cancel these nonlinearities using Feedback Linearization. In this paper the authors demonstrate an intelligent parameter estimation approach using structured artificial neural networks that continually "learns" the nonlinear parameter variations of a quarter-car suspension model. This estimation algorithm becomes the foundation for an Intelligent Feedback Linearization (IFL) controller for active vehicle suspensions. Results are presented for computer simulations, real-time experimental tests, and field evaluations using an off-road vehicle (a military HMMWV). Experimental results for a quarter-car test rig demonstrate 60% improvements in ride quality relative to baseline (non-adapting) control algorithms. Field trial results reveal 95% reductions in absorbed power and 65% reductions in peak sprung mass acceleration using this IFL approach versus conventional passive suspensions. [DOI: 10.1115/1.1408945]

1 Introduction

Researchers at the University of Texas Center for Electromechanics (UT-CEM) have been involved in the development of active suspension systems for off-road military vehicles since 1993 [1]. A major contribution of this research has been the development of linear electromechanical (EM) actuators that serve as force control elements in active suspensions [2]. These EM actuators were designed to retrofit into the existing suspension space of a military HMMWV, and are installed in parallel with a soft spring for static load support (Fig. 1). They are electronically controlled to provide bidirectional forces within a nominal range of ±2000 lb. These high-performance actuators introduce considerable opportunities for improving the ride quality, handling performance, and safety of off-road vehicles through the control of suspension forces.

The design of controllers for active vehicle suspensions has been the focus of numerous research publications in recent years [1,3–12]. Typically, these research contributions are theoretical in nature and rely on linear, time-invariant suspension models for controller design and simulated performance evaluation. However, suspension forces are inherently nonlinear, particularly for off-road vehicles. Off-road vehicles experience large suspension displacements, where the nonlinear kinematics and damping characteristics (Fig. 2) are significant.

These nonlinearities tend to degrade the performance of active suspension systems, introducing harshness to the ride quality and reducing off-road mobility. In addition, the dynamic characteristics of suspension components are not time-invariant, but are subject to change during a vehicle's life cycle. In light of these facts, it is worthwhile to consider a control approach that accounts for dynamic nonlinearities and responds to time-varying parameters.

While there are many techniques available for estimating the parameters of linear system models using input/output data, there are considerably fewer techniques available for estimating the structure of nonlinear systems [13,14]. A common approach is to assume a model structure that is nonlinear in the states, but is
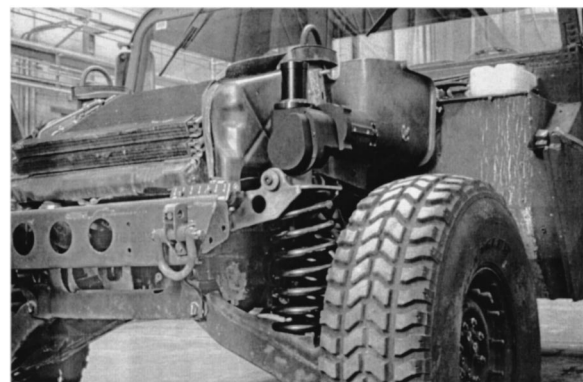

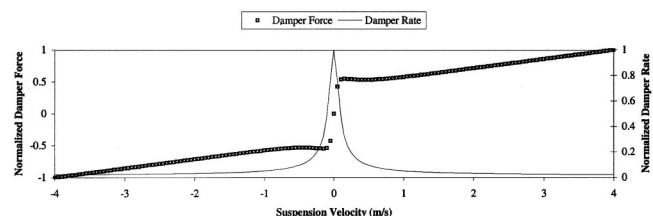**Fig. 1 EM actuator mounted on HMMW**

Fig. 2 Typical nonlinear suspension damping characteristics

linear in the parameters (e.g., $\dot{x} = a_1x + a_2x^2 + a_3x^3 + \ldots$). A model of this form allows for the use of least squares techniques (or recursive least squares for on-line estimation) to determine the unknown model parameters from system data [13–15,5,10]. A major drawback of this approach is that the structure of each nonlinearity must be specified in advance, using physical modeling or intuition. Another common approach is to treat the nonlinear dynamics as a "black box," and use high-order regression or Artificial Neural Networks (ANNs) to emulate their effects [7,8,13,14]. In the first case, an accurate physical model may be difficult to derive for nonlinear, time-varying systems. In the second case, the black box structure provides little or no physical insight into the system dynamics. Therefore, it is worthwhile to utilize a technique that combines the physical insight of linear, lumped-parameter modeling with the flexibility of the nonlinear black box approach.

This paper describes an Intelligent Feedback Linearization (IFL) controller that "learns" the nonlinear dynamics of a vehicle suspension and uses this information to control suspension forces. The nonlinear dynamics are modeled using a linear parameter varying (LPV) model structure. The parameters of this model are estimated on-line, and are used to update the controller gains at each time step. The result is a high-performance, real-time control algorithm that impoves the ride quality and predictability of the suspension response.

II Intelligent Control

Intelligence, as defined by Webster's Dictionary [16], implies the ability to **respond** successfully to a new experience and **learn** or understand from previous experiences. For a control system to be intelligent, it must possess two distinct characteristics:

- the ability to successfully adapt (or **respond**) to changes in its environment (time-varying plant parameters, unmodeled plant dynamics, etc) such that overall system performance is improved
- the ability to retain (or **learn**) this adaptive information for future reference

Thus, an intelligent controller can be defined as an adaptive controller with the ability to retain or "learn" information related to previous adaptive experiences.

Artificial Neural Networks (ANNs) are frequently used to provide this learning capability, though it is important to note that not all ANN-based control systems satisfy this definition of intelligence. ANNs are highly interconnected data processing elements typically used for function approximation and pattern recognition [17]. They are documented as being self-adapting "universal approximators" because of their ability to model any nonlinear function to any desired level of accuracy, given enough neurons [18,19]. In the context of intelligent control, ANNs can be used to estimate the parameters of a dynamic model in real-time, even if the plant is highly nonlinear and time-varying.

One specific type of ANN, the Radial Basis Function Network (RBFN), is well suited to the task of real-time system identification for two reasons. First, the network uses localized activation functions (radial basis functions), and thus learns information in a very localized fashion. As a result, parameter estimates obtained from a small region of the plant operating space do not adversely affect estimates from other operating regions. Second, the interconnection weights (which are self-adjusted during learning) are applied linearly on the output side of the network. This feature results in significantly reduced computational requirements for the RBFN, making it well-suited for real-time implementation.

A Indirect Adaptive (Self-Tuning) Intelligent Control. A large number of control architectures satisfy the definition of intelligence presented earlier in this section. One such architecture, the Indirect Adaptive Intelligent Controller (Fig. 3), is essentially
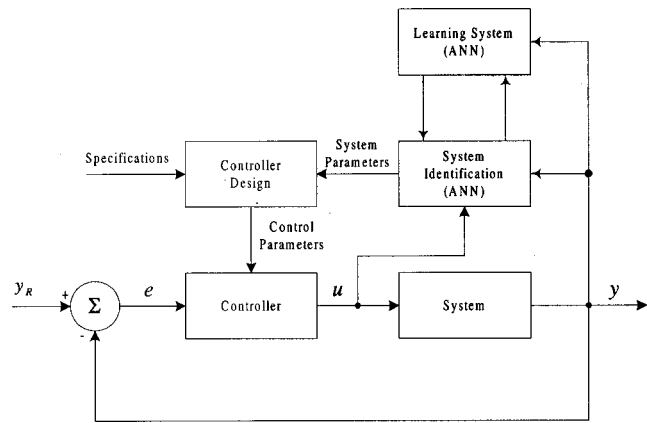

Fig. 3 The indirect adaptive intelligent control architecture

an extension of the self-tuning adaptive controller described by Åström and Wittenmark [15,20].

This controller is adaptive, as controller gains are updated on-line so that overall system performance is improved. The term "indirect" refers to the fact that gains are adapted as an indirect result of updated model parameters. The controller is intelligent, as model parameters are estimated and "learned" by an ANN. At each sample time, the ANN re-estimates the model parameters, using new and previously learned information. These parameters are used to recompute the controller gains, which are implemented in the controller.

III Intelligent Suspension Control Via Feedback Linearization

A standard assumption in the design of controllers for active vehicle suspension systems is that the vertical suspension dynamics can be modeled using four independent quarter-car models (Fig. 4) [4]. Although these models are typically assumed to be linear [4], the intelligent controller development presented here assumes that the stiffness and damping term k_s and b_s depend nonlinearly on the relative suspension travel, $\Delta = y_w - y_b$, and relative suspension velocity, $\dot{\Delta} = \dot{y}_w - \dot{y}_b$.
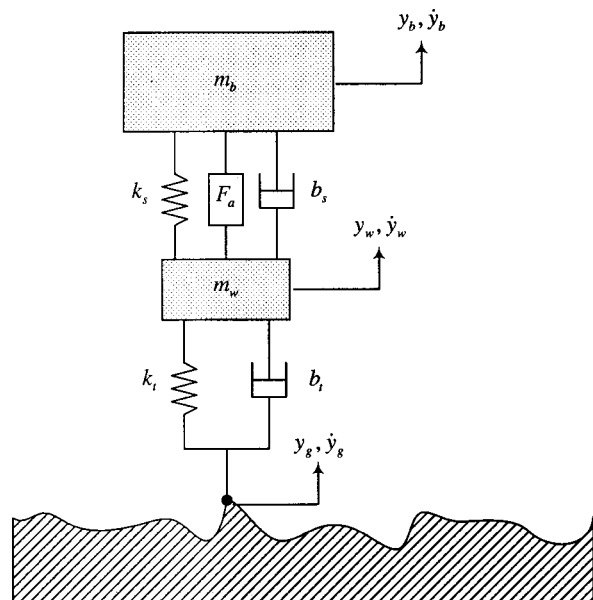

Fig. 4 Fourth-order quarter-car suspension model

One means of addressing the kinematic and damping nonlinearities in the design of active suspension controllers is through the application of Feedback Linearization [21]. A Feedback Linearizing controller is designed in three basic steps:

1 Identify the nonlinearities in the system
2 Cancel the nonlinearities
3 Apply a control action that gives a desired linear system response

Thus, Feedback Linearization transforms a system with nonlinear dynamics into one with linear dynamics so that more tractable linear techniques can be used to design the controller. The development of a Feedback Linearizing controller for the fourth-order, quarter-car suspension model is described next.

A Standard Feedback Linearization. Consider a nonlinear dynamic system described by differential equations in *controllable canonical form* [21]:

$$\frac{d^n x}{dt^n} = f(\mathbf{x}) + g(\mathbf{x})u \tag{1}$$

where $\mathbf{x} = [x, dx/dt, \ldots d^{n-1}x/dt]$ is the n-dimensional state vector, y is the scalar input, $f(\mathbf{x})$ and $g(\mathbf{x})$ are nonlinear functions of the state vector, $g(\mathbf{x})$ is invertible. It is easy to show [21] that the input u that linearizes the above system is:

$$u = g(\mathbf{x})^{-1}(u_L - f(\mathbf{x})) \tag{2}$$

Resulting in the transformed linear system:

$$\frac{d^n x}{dt^n} = u_L \tag{3}$$

where u_L is the linear control input used to specify the desired dynamics of the system. In other words, the control input u is composed one term that cancels the nonlinear plant dynamics and another provides the desired linear dynamics. Now consider the dynamics of a fourth-order, nonlinear, quarter-car model (Fig. 4):

$$m_b \ddot{y}_b(t) = b_s(\dot{\Delta}) \cdot \dot{\Delta}(t) + k_s(\Delta) \cdot \Delta(t) + F_a$$

$$m_w \ddot{y}_w(t) = -b_s(\dot{\Delta} \cdot \dot{\Delta}(t)) - k_s(\Delta) \cdot \Delta(t)$$

$$+ b_t \cdot (\dot{y}_g(t) - \dot{y}_w t) + k_t \cdot (y_g(t) - y_w(t)) - F_a \tag{4}$$

This system, with a relative damping coefficient that depends nonlinearly on suspension velocity $b_s(\dot{\Delta})$ and a relative stiffness coefficient that depends nonlinearly on suspension travel $k_s(\Delta)$, is an ideal candidate for Feedback Linearization. Let the scalar actuator force F_a be composed of two parts, $F_a = F_{a1} + F_{a2}$. If the constitutive relations $b_s(\dot{\Delta})$ and $k_s(\Delta)$ are known exactly, the nonlinear forces associated with these parameters can be canceled with the actuator control force:

$$F_{a1} = -b_s(\dot{\Delta}) \cdot \dot{\Delta}(t) - k_s(\Delta) \cdot \Delta(t) \tag{5}$$

Resulting in the transformed linear system:

$$\ddot{y}_b(t) = \frac{F_{a2}}{m_b}$$

$$\ddot{y}_w(t) = \frac{1}{m_w} \cdot (b_t \cdot (\dot{y}_g(t) - \dot{y}_w(t)) + k_t \cdot (y_g(t) - y_w(t)) - F_{a2}) \tag{6}$$

The last step is to define the desired suspension dynamics via actuator force F_{a2}, which corresponds to the u_L term in Eq. (3). F_{a2} can be constructed to implement a variety of linear control laws commonly used in active suspension systems [3–12]. For the implementation presented in this paper, the actuator force F_{a2} was chosen to be a linear combination of absolute sprung mass velocity (a "skyhook" damping term [3]) and relative displacement (an "effective spring rate" term [9,11]). For a given control law, the stability of the suspension's internal dynamics (i.e., the wheel hop mode) can be verified by analysis of the system eigenvalues [21,22].
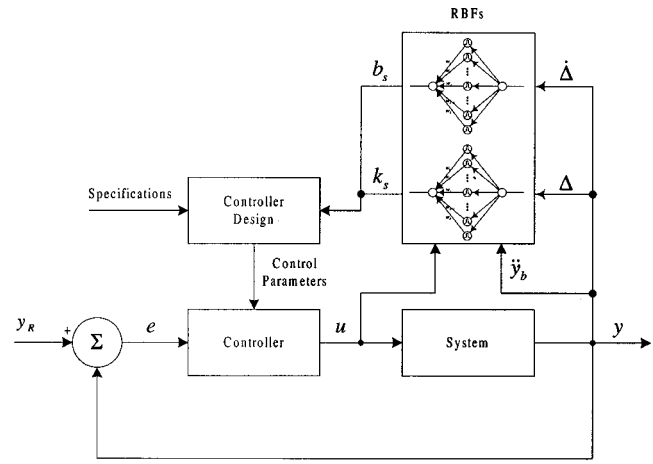

Fig. 5   Intelligent feedback linearization block diagram

B Intelligent Feedback Linearization (IFL). The IFL controller combines on-line, ANN-based parameter estimation with the standard Feedback Linearization control law of Eq. (6). The structure of this intelligent controller, as it relates to the active vehicle suspension system, is shown in the block diagram of Fig. 5.

The nonlinear suspension parameters $b_s(\dot{\Delta})$ and $k_s(\Delta)$ are estimated ("learned") in real-time using the Radial Basis Function Networks (RBFNs) described earlier. At each sample time, the values of Δ and $\dot{\Delta}$ are measured, the RBFNs are trained, and instantaneous parameter estimates $\hat{b}_s(\dot{\Delta})$ and $\hat{k}_s(\Delta)$ are used to compute the cancellation forces according to Eq. (5). Obviously, the computed cancellation forces will not be accurate when the system is initialized. However, with adequate training and sufficient excitation, the RBFNs will generate increasingly accurate parameter estimates, and the IFL controller will do a better job of canceling system nonlinearities.

IV Intelligent System Identification: Derivation of Equations

Previously, a fourth-order dynamic model, Eq. (4), was presented for the quarter-car model of Fig. 4. The first equation, representing the sprung mass dynamics $y_b(t)$, is rewritten to facilitate the derivation of parameter estimation equations:

$$\ddot{y}_b(t) = \frac{1}{m_b}(k_s(\Delta) \cdot \Delta + b_s(\dot{\Delta}) \cdot \dot{\Delta} + F_a) \tag{7}$$

This equation has tractable appeal because it represents a linear dynamic model with state-dependent parameters $k_s(\Delta)$ and $b_s(\dot{\Delta})$. Additionally, relative displacement $\Delta(t)$, relative velocity $\dot{\Delta}(t)$, and sprung mass acceleration $\ddot{y}_b(t)$ are all easily acquired using inexpensive sensing equipment. Although $k_s(\Delta)$ and $b_s(\dot{\Delta})$ are assumed to be nonlinear functions of relative displacement and velocity, these constitutive relations could have been formulated using any measurable system data.

Before implementing Eq. (7) for real-time parameter estimation, it is important to understand the limitations on its use. While the inclusion of actuator force F_a is necessary for identification purposes, it can be a liability when based on output feedback. If this control force is solely dependent on relative suspension displacement or velocity, the parameter estimation equations can become indeterminate. For this reason, the actuator force input should be sufficiently independent, so that it is not strongly correlated to either the relative displacement or velocity.

Separate RBFNs were constructed to learn the constitutive relations of each parameter (Fig. 6), leading to a naturally modular or "structured" neural network [17,23], which combined the in-
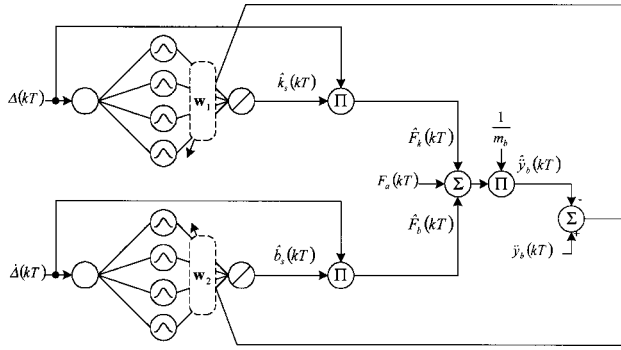
Fig. 6 RBFN structure for intelligent system identification

tuitive appeal of physics-based models with the "universal function approximating" capability of ANNs. Although Eq. (7) represents a continuous-time model of the sprung mass dynamics, the estimation process required a discrete-time form of this model. Specifically, discrete-time measurement of relative displacement $\Delta(kT)$, relative velocity $\dot{\Delta}(kT)$, and sprung mass acceleration $\ddot{y}_b(kT)$ were required to generate discrete-time estimates $\hat{k}_s(\Delta)$ and $\hat{b}_s(\dot{\Delta})$, where T denotes the sample interval and "^" notation denotes an estimated value. Instantaneous spring force estimates $\hat{F}_k(kT)$ and damping force estimates $\hat{F}_b(kT)$, used to compute the instantaneous sprung mass acceleration estimate $\hat{\ddot{y}}_b(kT)$, are also shown in the figure.

Because there are two distinct networks in the structured model of Fig. 6, two distinct weight update equations were implemented for training. In each case, the update equations were formulated so that training proceeds in the negative gradient of the error cost function $J(e)$, which is defined based on the error between the actual sprung mass accelerations $\ddot{y}_b(kT)$ and the predicted sprung mass accelerations $\hat{\ddot{y}}_b(kT)$:

$$e(kT) = \ddot{y}_b(kT) - \hat{\ddot{\gamma}}_b(kT)$$

$$J(e) = \frac{1}{2N} \sum_{k=1}^{N} e(kT)^2 \tag{11}$$

The output weights $\mathbf{w}_1$ and $\mathbf{w}_2$ are associated with the $\hat{k}_s(\Delta)$ and $\hat{b}_s(\dot{\Delta})$ networks, respectively. The activation functions associated with each RBFN are distributed uniformly across the input range for each network. For each discrete-time sample $(\Delta(kT)),\dot{\Delta}(kT)$, the structured RBFN's outputs are:

$$\hat{k}_s(\Delta) = y_1(\Delta(kT)) \cdot \mathbf{w}_1$$

$$\hat{b}_s(\dot{\Delta}) = y_2(\dot{\Delta}(kT)) \cdot \mathbf{w}_2 \tag{12}$$

$$\hat{\ddot{y}}_b(kT) = \left(\frac{1}{m_b} (\hat{k}_s(\Delta) \cdot \Delta((kT)) \right.$$

$$\left. + \hat{b}_s(\dot{\Delta}) \cdot \Delta((kT)) + F_a(kT)) \right)$$

Errors $e(kT)$ are backpropagated to obtain the weight update equations:

$$\mathbf{w}_1(kT) = \mathbf{w}_1(kT) - \eta_1 \cdot \frac{\partial J(e)}{\partial \mathbf{w}_1}$$

$$= \mathbf{w}_1(kT) + \frac{\eta_1}{m_b} \cdot e(kT)$$

$$\cdot \Delta(kT) \cdot y_1(\Delta(kT))$$

$$\mathbf{w}_2(kT) = \mathbf{w}_2(kT) - \eta_2 \cdot \frac{\partial J(e)}{\partial \mathbf{w}_2} \tag{13}$$

$$= \mathbf{w}_2(kT) + \frac{\eta_2}{m_b} \cdot e(kT)$$

$$\cdot \dot{\Delta}(kT) \cdot y_2(\dot{\Delta}(kT))$$

V Intelligent System Identification: Off-Line Experimental Results

As stated in the introductory sections, this research was conducted as part of the University of Texas Center for Electromechanics (UT-CEM) Electromechanical Suspension (EMS) program, which is developing electromechanical actuators for active vehicle suspension systems [1,2,9,11,12]. Currently, UT-CEM has a quarter-car test rig to test advanced EMS control algorithms. The test rig, shown in Fig. 7, was designed to have dynamic characteristics comparable to a military HMMWV.

For the experimental evaluations, data collected from the test rig was used to quantify the effectiveness of the intelligent system identification algorithm. Specifically, dynamic measurements from the test rig were used to train the RBFN's off-line (Eqs. (11)–(13)), and determine the nonlinear variations in suspension damping $b_s(\dot{\Delta})$ and suspension stiffness $k_s(\Delta)$. First, the quarter-car test rig was excited using a hydraulically-actuated terrain input $y_g(kT)$, and the resulting suspension displacement $\Delta(kT)$ and sprung-mass acceleration $\ddot{y}_b(kT)$ were acquired at a sampling rate of 200 Hz. A swept sinusoid input profile, with a frequency range of $0.1 \leq f_g \leq 25.0$ Hz and 0.025 m amplitude, was selected for the terrain input to ensure adequate excitation of the system's vertical dynamics. The data revealed a resonant frequency for the sprung mass at 1.4 Hz, and a resonant frequency for the unsprung mass at approximately 5.0 Hz (Fig. 8).

Next, the experimental vehicle response data was sub-sampled to obtain input/output training and testing data for the RBFN's. The RBFN training equations (Eqs. (11)–(13)) were implemented using the experimental response data. The RBFN weights and the adaptation parameters η_1 and η_2 were initialized to ensure rapid, yet stable, convergence during training. The initial (untrained) error cost function $J(e)$ of the testing data was 0.030. Training continued until the error cost function leveled off at 0.007 after 1000 training epochs.
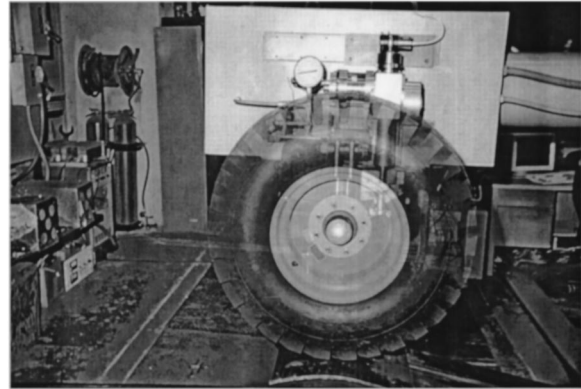

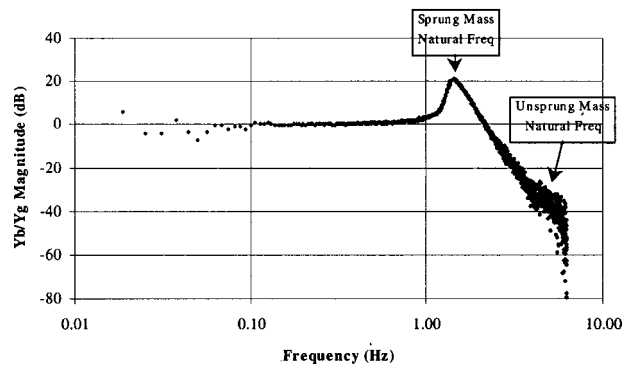**Fig. 7 UT-CEM quarter-car test rig**

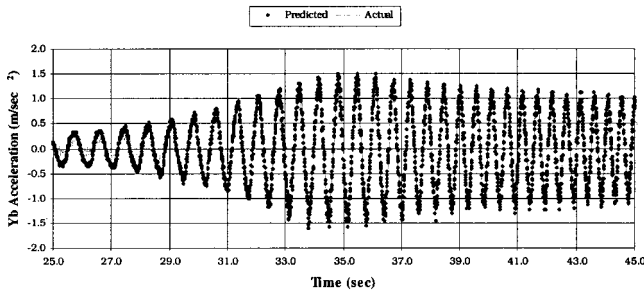**Fig. 8 Magnitude versus frequency diagram of the collected data**

Fig. 9 Swept sine wave input experimental results

At this point, the network's predictions of sprung mass acceleration $\hat{\ddot{y}}_b(kT)$ were very reasonable approximations to the "actual" measured accelerations $\ddot{y}_b(kT)$, as shown in Fig. 9. Figure 10 compares the estimated variation of suspension stiffness with "actual" measurements made on the quarter-car test rig. Because the range of suspension travel was relatively small (± 0.03 m), the spring rate was relatively constant. The wide spread in measured stiffness is primarily due to hysteresis in the suspension, as stiffness magnitudes were found to be dependent on the direction of suspension travel (which was not an input to the RBFN). Figure 11 shows the estimated variation of damping as a function of relative suspension velocity. No suitable technique could be devised to experimentally validate this variation, but the trend is in agreement with characteristics reported in the literature [24].

The results of this intelligent system identification experiment illustrates two main points. First, they demonstrate that the structured RBFNs can accurately model the nonlinear dynamics of a quarter-car suspension system. More importantly, they provide very reasonable estimates of parameter variations on an actual suspension with unknown characteristics. Although this demonstration was performed off-line, the next section details the extension to real-time, closed-loop identification
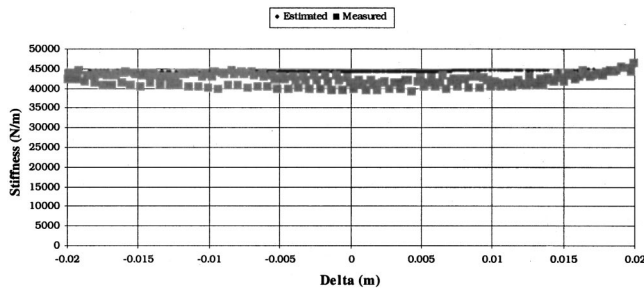

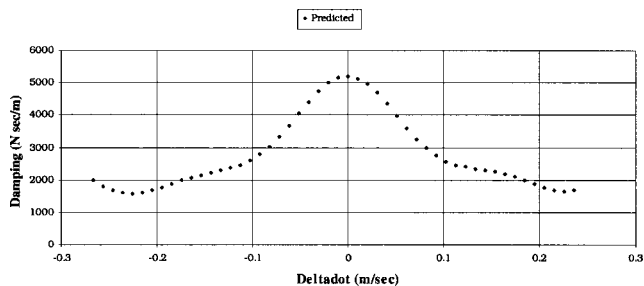Fig. 10 Experimental stiffness identification results

Fig. 11 Experimental damping identification results

VI Intelligent Feedback Linearization: Real-Time Experimental Results

In the previous section, the effectiveness of off-line intelligent parameter estimation was demonstrated. Although the results were promising, the real potential of this technique lies in its application to real-time control. In this section, experimental results are presented for real-time, closed-loop intelligent control. The consequences of "closing the loop" and performing system identification at 1000 Hz presented two new technical challenges. First, the presence of output feedback tended to destabilize the estimation process, especially when the control signal was a linear combination of the input data (suspension displacement and velocity). Second, completing the estimation and control calculations in less than 1 millisecond required highly specialized control hardware and software.

To experimentally assess the performance of real-time intelligent suspension control, the UT-CEM quarter-car test rig (Fig. 7) was again used. The IFL control law of Eqs. (5) and (6) was combined with a real-time implementation of the RBFN training equations (Eqs. (11)–(13)) to create a self-adapting active suspension controller. In this configuration, the RBFN provided instantaneous estimates of suspension stiffness and damping, so that nonlinear dynamics could be canceled and replaced with the desired linear dynamics. The effectiveness of this approach was measured by comparing sprung mass response to terrain inputs using standard (nonintelligent) and intelligent control laws.

The quarter-car test rig was equipped with dSpace® hardware and software to manipulate amplifier current for the EM actuator. A baseline control law was designed using a combination of skyhook damping [3] and sprung mass proportional control, resulting in a Proportional+Derivative (PD) control of sprung mass position. This control law was programmed in Simulink®, compiled and downloaded to the dSpace® hardware, and executed at a "real-time" rate of 1000 Hz.

Next, the quarter-car test rig was excited using a hydraulically-actuated terrain input $y_g(kT)$, chosen to simulate 0.07 m (2.75 in.) peak-to-peak off-road conditions at 64.5 kph (40 mph) (Fig. 12). The resulting suspension displacement $\Delta(kT)$ and sprung mass acceleration $\ddot{y}_b(kT)$ were acquired as part of the controller implementation. Sprung mass position $y_b(kT)$ was measured using a linear encoder, and was acquired and differentiated for control purposes.

The baseline controller gains were tuned to achieve an absolute (skyhook) damping rate of 15277 N·s/m (87 lb·s/in) and an absolute sprung rate of 97736 N/m (558 lb/in). These gains resulted in very significant reductions in sprung mass response (less than 0.0125 m (0.5 in.) peak-to-peak, an 81% amplitude reduction), as shown in the first 30 seconds of Fig. 13. While the baseline algorithm was controlling the active suspension system, the intelligent system identification algorithm was allowed to train using real-time input/output data. Thus, at each control interval, the RBFN training equations (Eqs. (11)–(13)) were executed using instantaneous measurements of suspension displacement $\Delta(kT)$, suspen-
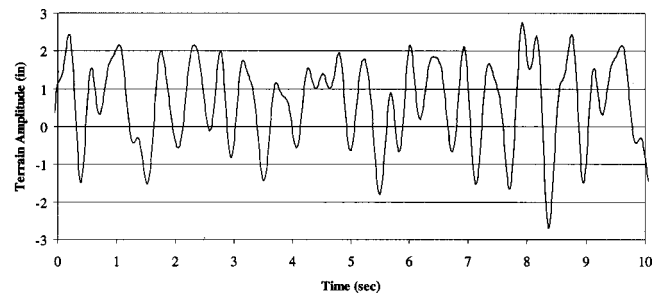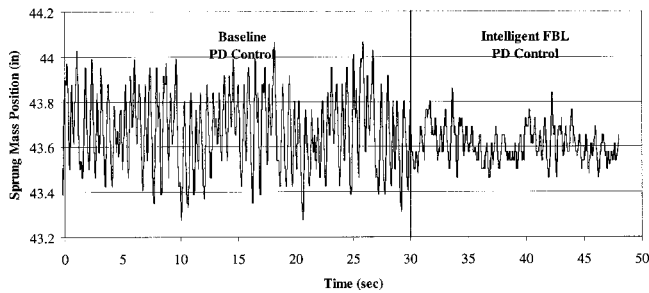

Fig. 12 Off-road terrain inputs for experimental control evaluations

Fig. 13 Sprung mass response baseline and intelligent FBL control

sion velocity $\dot{\Delta}(kT)$, actuator force $F_a(kT)$, and sprung mass acceleration $\ddot{y}_b(kT)$. The RBFN weights and the adaptation parameters η_1 and η_2 were initialized to ensure rapid, yet stable, convergence during training.

Finally, after 5 minutes of real-time training, the IFL controller was activated using the same controller gains as the baseline (fixed-gain) controller. Figure 13 shows the dramatic improvement in sprung mass response when the IFL controller was activated at 30 seconds. The IFL controller exhibited an additional 60% reduction in sprung mass displacement when activated. Recall that only difference in the two control laws was the cancellation of learned system nonlinearities by the IFL controller.

The results of this closed-loop experiment clearly demonstrate the improvements in performance that can be achieved using IFL, even for baseline PD control. The IFL controller significantly reduced the transmission of high-frequency forces to the sprung mass, translating to better ride quality for passengers and equipment. Also, these results provide conclusive evidence that the intelligent identification algorithm runs effectively in real-time and may be feasible for full-vehicle applications.

VII Intelligent Feedback Linearization: Real-Time HMMWV Implementation

As explained in the introductory sections of this paper, a military HMMWV was retrofitted with electromechanical actuators at each suspension element to improve ride quality and mobility for off-road terrains. The extension of quarter-vehicle system identification and control algorithms to a full-vehicle implementation was complicated by several factors. Most notably, the vertical dynamics at each corner of the sprung mass are coupled to other corners through rigid body modes (heave, pitch, and roll). Clearly, the utilization of quarter-vehicle algorithms (which neglect this coupling) on full-vehicle platforms is a simplification of the true vehicle dynamics, and will result in reduced performance. However, extensive computer simulations conducted at UT-CEM using full-vehicle, half-vehicle, and quarter-vehicle models suggested that such performance reductions (particularly those related to ride quality) were not substantial and could be justified by the reduced complexity of implementation. These findings are consistent with previous research, and resulted in implementation of these quarter-car algorithms. Current research at UT-CEM is investigating the adoption of a fully coupled dynamic model (14th-order) for system identification and control, particularly with respect to handling performance.

Preliminary field evaluations focused on parameter estimation and IFL control (based on quarter-car algorithms) to improve ride quality, as measured by the U.S. Army "absorbed power" index (AMM-75 Ground Mobility Model) [25]. This ride quality standard uses weighted filtering of sprung mass acceleration to quantify the rate of energy absorbed by human occupants, and limits this value to 6.0 W. For these tests, two military HMMWVs, one equipped with a standard passive suspension and one equipped with the active electromechanical suspension, were
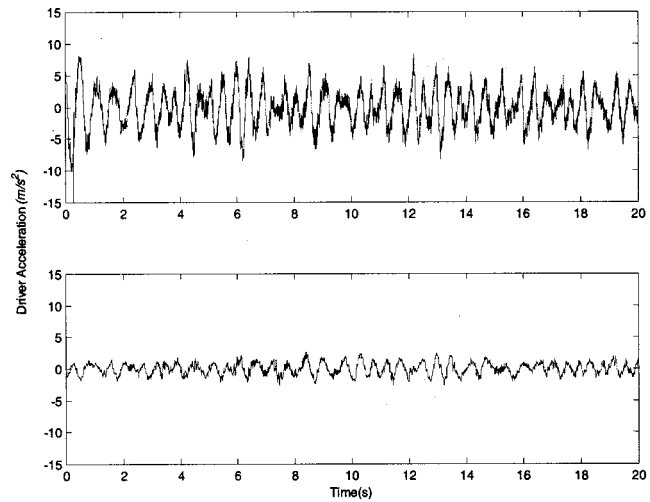
Fig. 14 Sprung mass accelerations for passive HMMWV suspension (top) and active HMMWV suspension with IFL control (bottom)—0.04 m RMS terrain at 24.1 kph (15 mph)

driven over a variety of off-road test courses at the U.S. Army's Yuma Proving Ground. The baseline control law was a nonadapting, independent (nonmodal) combination of skyhook damping [3] and spring cancellation [1,9,11,12]. Over a period of several hours, real-time data was collected from all four suspension elements and used to train the RBFNs. Thus, at each control interval, the RBFN training equations (Eqs. (11)–(13)) were executed using instantaneous measurements of suspension displacements $\Delta_i(kT)$, suspension velocities $\dot{\Delta}_i(kT)$, actuator forces $F_{ai}(kT)$, and sprung mass accelerations $\ddot{y}_b(kT)$. These parameter estimates were updated at each control interval and utilized by the IFL control law (Eqs. (5) and (6)).

Figure 14 compares the vertical acceleration measurements (at the sprung mass center of gravity) for the HMMWV with standard passive suspension (top) and active suspension (bottom). Each HMMWV was professionally driven across a straight-line washboard terrain (0.04 m RMS) at 24.1 kph (15 mph). The passive response exhibits peak accelerations in excess of 80 m/s², and absorbed power of 6.64 W, which exceeds the 6.0 W threshold [25]. Peak accelerations for the active suspension are below 3.0
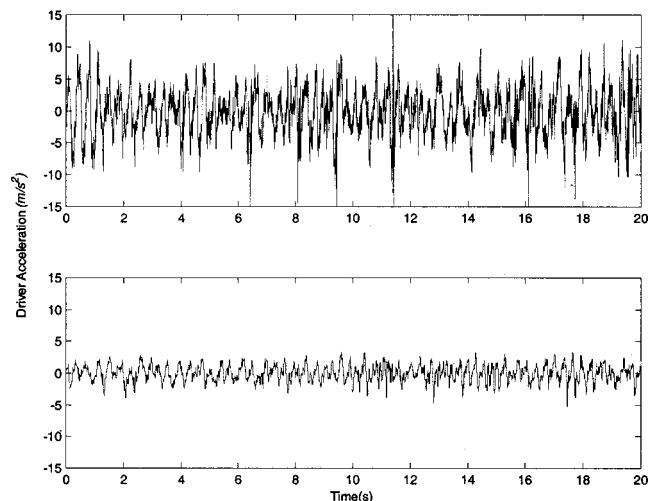
Fig. 15 Sprung mass accelerations for passive HMMWV suspension (top) and active HMMWV suspension with IFL control (bottom)—0.04 m RMS terrain at 40.2 kph (25 mph)

m/s^2, and the absorbed power is an incredibly low 0.35 W (a 95% reduction). Figure 15 is a similar comparison for 40.2 kph (25 mph). The passive response (top) exhibits peak accelerations in excess of 15.0 m/s^2, and absorbed power of 13.85 W, more than twice the limiting threshold [25]. Peak accelerations for the active suspension are below 5.0 m/s^2, and the absorbed power is a remarkably low 1.49 W (an 89% reduction).

VIII Conclusions and Recommendations

This paper details the development and real-time implementation of intelligent parameter estimation and Intelligent Feedback Linearization (IFL) to improve the ride quality and handling performance of off-road active suspension systems. The IFL controller combines Radial Basis Function Networks (RBFNs) with an adaptive control strategy to cancel undesired nonlinearities, thus facilitating the use of linear control laws. Experimental results from a quarter-car test rig demonstrate 60% improvements in ride quality relative to a baseline (non-adapting) controllers. Additional, field trial results from a HMMWV implementation clearly demonstrate the performance of quarter-vehicle parameter estimation and control algorithms for improved ride quality. 95% reductions in absorbed power and 65% reductions in peak sprung mass acceleration have been documented using this IFL approach.

The IFL controller design followed a logical progression from concept and computer simulation [26], to real-time experiment, to full-vehicle implementation. Testing and refinement of the full-vehicle controller, currently installed on a HMMWV, is still underway. Current research at UT-CEM is addressing full-vehicle (dynamically coupled) control algorithms and bump-stop avoidance algorithms, as the energy transmitted to occupants relies heavily on avoiding the shocks associated with travel space exhaustion.

References

[1] Beno, J. H., Bresie, D. A., Ingram, S. K., Weeks, D. A., and Weldon, Wm. F., 1995, "Electromechanical Suspension System," Final Report to U. S. Army Tank and Automotive Command, Warren, MI, June.

[2] Weeks, D. A., Beno, J. H., Guenin, A., and Bresie, D. A., 1999, "The Design of an Electromagnetic Linear Actuator for an Active suspension," SP-1438, Steering and Suspension Technology Symposium 1999, SAE, Warren, MI.

[3] Crosby, M., and Karnopp, D. C., 1973, "The Active Damper—A New Concept for Shock and Vibration Control," Shock and Vibration Bulletin, Part H.

[4] Hrovat, D., 1997, "Survey of Advanced Suspension Developments and Related Optimal Control Applications," Automatica **33**, No. 10, pp. 1781–1817.

[5] Kim, E. S., 1996, "Nonlinear Indirect Adaptive Control of a Quarter Car Active Suspension," Proceedings of the 1996 IEEE International Conference on Control Applications, pp. 61–66.

[6] Williams, D. E., and Haddad, W. M., 1997, "Active Suspension Control to Improve Vehicle Ride and Handling," Vehicle System Dynamics **28**, No. 1, pp. 1–24.

[7] Moran, A., and Nagai, M., 1994, "Optimal Active Control of Nonlinear Vehicle Suspensions Using Neural Networks," JSME International Journal, Series C **37**, No. 4, pp. 707–719.

[8] Nagai, M., Moran, A., Tamura, Y., and Koizumi, S., 1997, "Identification and Control of Nonlinear Active Pneumatic Suspension for Railway Vehicles, Using Neural Networks," Control Engineering Practice **5**, No. 8, pp. 1137–1144.

[9] Scheutze, K. T., Beno, J. H., Weldon, W. F., and Sreenivasan, S. V., 1998, "A Comparison of Controller Designs for an Active, Electromagnetic, Offroad Vehicle Suspension System Traveling at High Speed," presented at the SAE International Congress and Exposition, Detroit, MI, Feb. 23–26.

[10] Sunwoo, M., and Cheok, K. C., 1991, "Investigation of Adaptive Control Approaches for Vehicle Active Suspension Systems," Proceedings of 1991 American Control Conference, Vol. 2, pp. 1542–1547.

[11] Weeks, D. A., Beno, J. H., Bresie, D. A., and Guenin, A. M., 1997, "Control System for Single Wheel Station Tracked Vehicle Active Electromagnetic Suspension," presented at SAE International Congress and Exposition, Detroit, MI, Feb.

[12] Weeks, D. A., Beno, J. H., Bresie, D. A., and Guenin, A. M., 1997, "Laboratory Testing of Active Electromagnetic Near Constant Force Suspension (NCFS) Concept on Subscale Four Corner, Full Vehicle Test-Rig," presented SAE International Congress and Exposition, Detroit, MI, February 24–27.

[13] Ljung, L., 1991, "Issues in System Identification," IEEE Control Syst. Mag., pp. 25–29.

[14] Ljung, L. and Glad, T., 1994, *Modeling of Dynamics Systems*, Prentice Hall.

[15] Aström, K. J., and Wittenmark, B., 1995, *Adaptive Control*, 2nd Ed., Addison Wesley.

[16] G. C. Merriam Co., 1991, *Webster's New Collegiate Dictionary*, G. C. Merriam Co.

[17] Haykin, S., 1994, *Neural Networks, A Comprehensive Foundation*, Prentice Hall.

[18] Cybenko, G., 1989, "Approximations by Superpositions of a Sigmoidal Functions," Mathematics of Control Signal Systems 2 pp. 303–314.

[19] Hornik, J., Stinchcombe, M., and White, H., 1989, "Multilayer Feedforward Networks are Universal Approximators," Neural Networks **2**, pp. 359–366.

[20] Baker, W. L., and Farrell, J. A., 1992, *An Introduction to Connectionist Learning Control Systems, Handbook of Intelligent Control: Neural, Fuzzy, and Adaptive Approaches*, Van Nostrand Reinhold.

[21] Slotine, J. J., and Li, W., 1991, *Applied Nonlinear Control*, Prentice Hall.

[22] Brogan, W. L., 1991, *Modern Control Theory*, 3rd ed., Prentice Hall.

[23] Bruzzone, L., Roli, F., and Serpico, S. B., 1998, "Structured Neural Networks for Signal Classification," Signal Process. **64**, No. 3, pp. 271–290.

[24] Bastow, D., and Howard, G. P., 1993, *Car Suspension and Handling*, 3rd Ed., Society of Automotive Engineers, Inc.

[25] Wong, J. Y., 1993, *Theory of Ground Vehicles*, Wiley, New York, NY.

[26] Buckner, G. D., and Schuetze, K. T., 1999, "Intelligent Estimation of System Parameters for Active Vehicle Suspension Control" SP-1438, Steering and Suspension Technology Symposium 1999, SAE, Warren, MI.

Point-to-Point Motion Planning for Servosystems With Elastic Transmission Via Optimal Dynamic Inversion[1]

Aurelio Piazzi
Dipartimento di Ingegneria dell'Informazione,
University of Parma, Parma, Italy
e-mail: aurelio@ce.unipr.it

Antonio Visioli
Dipartimento di Elettronica per l'Automazione,
University of Brescia,
Via Branze 38, I-25123 Brescia, Italy
e-mail: visioli@bsing.ing.unibs.it

A new technique, based on dynamic inversion, for the residual vibration reduction in the point-to-point motion of servosystems with elastic transmission is presented. The methodology consists of defining a suitable motion law for the load, and subsequently determining, via dynamic inversion, the corresponding command function for the system. The method inherently assures the robustness of the control scheme despite inaccuracies in the estimation of the stiffness constant and of the damping of the transmission. The main contribution of the paper lies in the definition of a simple optimization procedure which allows the system inversion point that minimizes the residual vibration to be found. Experimental results show that in this way the identification phase is less critical and performances can be significantly improved.
[DOI: 10.1115/1.1408944]

1 Introduction

High performances servosystems might suffer from the presence of elasticities in the transmission, which produces a residual vibration at the end of a point-to-point motion. This fact introduces limitations in the reduction of the working cycle time, since the oscillation has to vanish before achieving the desired accuracy of the positioning system. This problem has been addressed by a number of researchers in the past and two strategies have been followed: either implementing a closed-loop control scheme, in which the state of the dynamic system has to be known during the motion (and therefore apposite sensors have to be adopted) or an open-loop control scheme which relies on an appropriate motion planning methodology. In the context of the open-loop strategy, the input shaping technique has been successfully developed over the last decade (see e.g. [1,2]). Basically, it consists of convolving a sequence of impulses, also known as the input shaper, with a desired system command to generate the system command that is then used to drive the system.

In a previous paper [3] we proposed an alternative approach to the input shaping technique. It is based on the concept of dynamic inversion and it allows minimization of the motion time while taking into account actuator constraints. The general idea is to first define an arbitrarily smooth closed-form polynomial motion function, parameterized by the time interval τ, for the load of the system to avoid oscillations during and at the end of the motion [4]. Then, by means of dynamic inversion the actual command input that causes the desired planned load motion is derived. Simulation and experimental results have proven the effectiveness of the method, with respect to the input shaping technique, and how it is inherently robust to modeling errors.

In this paper, we further develop the system-inversion-based methodology. Rather than considering a priori the uncertainties of the model, we perform a simple procedure to search for the optimal inversion point to minimize the residual vibration amplitude. In other words, starting from values of the system parameters determined by means of a simple identification experiment, we modify them in the system model adopted for the dynamic inversion, through repetitive experiments, until the residual vibration amplitude is minimized.

2 Dynamic Inversion Based Motion Planning

The presence of a gearbox in a mechanical positioning servosystem generally introduces an elastic element which can be simply described by the model shown in Fig. 1 where y is the coordinate representing the motor shaft displacement, x is the coordinate representing the mass displacement, m is the load mass, k the stiffness constant, and c the damping of the transmission [5]. The well-known linear relation between x and y has the following differential form:

$$m\ddot{x} + c\dot{x} + kx = c\dot{y} + ky \qquad (1)$$

which can be rewritten as:

$$\ddot{z} + 2\xi\omega_n\dot{z} + \omega_n^2 z = -\ddot{y}$$

where $z = x - y$, $\omega_n = \sqrt{k/m}$ rad·s^{-1} is the frequency of the oscillatory mode and $\xi = c/2m\omega_n$ is the damping ratio.
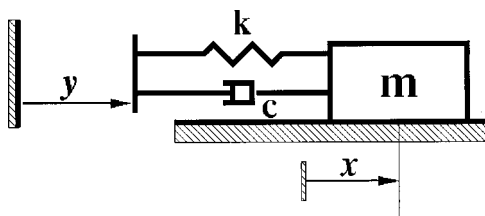

Fig. 1 Model of an elastic transmission

In general (we refer for example to the motion planning of industrial robot manipulators), the elasticity of the transmission is not taken into account and the motion is planned on y (the input of the system (1)), exploiting the full capabilities of the actuator and considering the mass m rigidly linked to the motor. When, however, excessive vibrations occur, the velocities, accelerations and jerks of the trajectory have to be reduced by increasing the motion time and therefore limiting the performances of the system. This drawback can be overcome by adopting a system-inversion-based methodology which will be briefly described in the following. For details see [3].

Define a point-to-point motion law from position 0 to q for the load in the time interval $[0,\tau]$ using the "transition" polynomials introduced in [4]:

$$x(t;\tau) = q \frac{(2h+1)!}{h!\,\tau^{2h+1}} \sum_{i=0}^{h} \frac{(-1)^{h-i}}{i!(h-i)!(2h-i+1)}\,\tau^i t^{2h-i+1}. \quad (2)$$

Outside the interval $[0,\tau]$, $x(t;\tau)$ is simply defined as $x(t;\tau)=0$ if $t \leq 0$ and $x(t;\tau)=q$ if $t \geq \tau$. In (2) the integer h can be arbitrarily chosen in order to assure $x(t;\tau) \in C^{(h)}$ over $\mathbb{R}$, i.e., $x(t;\tau)$ has continuous derivatives up to the hth order. Note that $x(t;\tau)$ is monotonically increasing and as a consequence, the planned motion of the mass m is, by construction, free of oscillatory modes.

Consider the transfer function of the system (1):

$$G(s) = \frac{X(s)}{Y(s)} = \frac{cs+k}{ms^2+cs+k} \qquad (3)$$

Applying the Laplace transform operator $\mathcal{L}$ both to $y(t;\tau)$ and $x(t;\tau)$, the closed-form expression of the parameterized input function for $t \geq 0$ (obviously $y(t;\tau)=0$ if $t<0$) which causes the desired output function can be calculated as:

$$y(t;\tau) = \mathcal{L}^{-1}[G^{-1}(s)X(s;\tau)] = \frac{m}{c}\dot{x}(t;\tau) + \left(1 - \frac{mk}{c^2}\right)x(t;\tau)$$

$$+ \frac{mk^2}{c^3} e^{-(k/c)t} \int_0^t e^{(k/c)v} x(v;\tau)dv. \qquad (4)$$

Note that $y(t;\tau)$ is all over bounded because the excited zero mode $e^{-(k/c)t}$ is stable. In order to obtain $y(t;\tau)$ belonging to $C^{(l)}$ it is necessary that, by virtue of (4), $x(t;\tau)$ belong to $C^{(l+1)}$, i.e., $h = l+1$. In particular, to at least ensure the continuity of the velocity input function, the constraint $h \geq 2$ must be satisfied.

At this point the optimization procedure described in [3] for the minimization of the motion time subject to actuator constraints can be readily applied.

3 Dynamic Inversion Point Optimization

In the previous section it has been exposed a dynamic inversion based synthesis of the motion input that depends, besides τ, on the parameters m, c, and k. In particular, the linkage parameters c and k, which are not exactly known in many practical cases, can be explicitly indicated as formal parameter arguments in $y(t;c,k,\tau)$. Thus, the problem of the optimal selection of $c \geq \delta_c$ and $k \geq \delta_k$ in $y(t;c,k,\tau)$ arises, where δ_k and δ_c are given arbitrarily small positive values of the natural frequency and of the damping ratio. We propose to choose c and k in order to minimize the amplitude of the actual residual vibration (the transient motion of the load for $t \geq \tau$). Application of input $y(t;c,k,\tau)$ to the actual servo determines an output motion denoted as $x(t;c,k,\tau)$. Hence, the residual vibration amplitude can be defined as:

$$J = J(c,k) := \max_{t \geq \tau} |x(t;c,k,\tau) - q|. \qquad (5)$$

The addressed motion planning problem is therefore posed as the following minimization problem:

$$\min_{c \ge \delta_c, k \ge \delta_k} J(c,k). \qquad (6)$$

Searching for a global solution of the optimization problem is extremely difficult because it has to be solved by means of suitably arranged experimental trials. Therefore, we propose a practicable local optimization procedure based on a simplified coordinate descent method [[6], p. 227] which is in any case capable to significantly improve the control system performances. Hence, the minimizers c^* and k^* of problem (6) can be found by means of the following optimal inversion point (OIP) procedure.

OIP Procedure

1 Perform an identification experiment and estimate k_0 and c_0 (initial values).

2 Set $k^* := k_0$, $c^* := c_0$, flag=0.

3 Perform an experiment and set $I := J(c^*, k^*)$ and $I^+ = I$.

4 Set $k^* = (1+\varepsilon)k^*$.

5 Perform an experiment and set $I := J(c^*, k^*)$.

6 If $I < I^+$ then set flag=1 and go to 3.

7 If flag=1 go to 11.

8 Set $k^* = (1-\varepsilon)k^*$. If $k^* < \delta_k$ then set $k^* = \delta_k$.

9 Perform an experiment and set $I := J(c^*, k^*)$.

10 If $I < I^+$ then go to 8.

11 Set flag=0.

12 Set $c^* = (1+\varepsilon)c^*$.

13 Perform an experiment and set $I := J(c^*, k^*)$.

14 If $I < I^+$ then set flag=1 and go to 12.

15 If flag=1 go to 19.

16 Set $c^* = (1-\varepsilon)c^*$. If $c^* < \delta_c$ then set $c^* = \delta_c$.

17 Perform an experiment and set $I := J(c^*, k^*)$.

18 If $I < I^+$ then go to 16.

19 End.

The typical identification experiment that can be performed at step 1 might consist of applying a torque impulse to the motor and analyzing the oscillatory response of the load. From the evaluation of the frequency and of the decay ratio of the response, the stiffness constant and the damping ratio can be straightforwardly determined.

Parameter ε determines the velocity of the descent to the minimum and the precision in determining k^* and c^*. It is easy to adapt it in order to have a fast descent to the minimum at the beginning and then increasing the accuracy once we are closed to it (for example, on the practical grounds, ε can be initially fixed to 0.05).

Remark 1. It is very important to stress that the resulting optimal parameters do not necessarily coincide with the real values of the parameters of the physical system. In other words, minimizing the residual vibration does not mean in general that we have accurately identified the stiffness constant and the damping ratio of the system, since nonlinear effects, which are inevitably present in the system, are not included in the simple model (1).

4 Experimental Setup and Results

The experimental setup consists of a testbed, depicted in Fig. 2, in which two carts, linked by a spring, slide on a stainless steel rectilinear guide (see Fig. 3 for a detail of the two carts). The first cart is connected to a belt which is moved through some pulleys by means of a brushless motor configured in torque mode, i.e., the signal given to the drive by the controller is a torque command. The overall reduction rate of the transmission system is known and therefore, we assume that the input reference function $y(t)$ is the position of the first cart, rather than the position of the motor shaft.

Then, the position $y(t)$ of the first cart is measured by means of an incremental encoder, mounted on the motor shaft, whose resolution is $4 \cdot 1000$ impulses per motor revolution. The second cart,
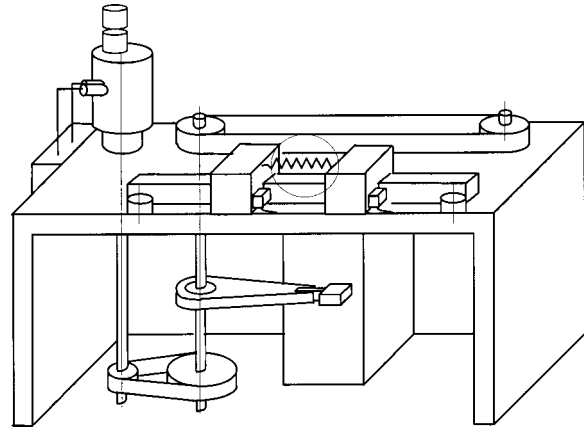

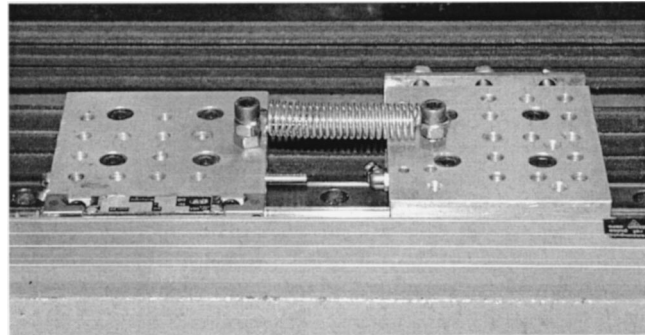**Fig. 2 Sketch of the experimental setup**

Fig. 3 The two carts linked with the spring adopted for the experiments

whose mass is 0.8 kg, is not actuated and its position $x(t)$ is measured with an incremental linear scale with a resolution of 40 μm.

The control system is implemented in a PC with I/O boards and the control frequency is 1 kHz. The position of the first cart is controlled by a standard Proportional-Integral-Derivative (PID) controller which has been accurately tuned by a trial and error procedure, in order to guarantee a very low positioning error during the motion.

A simple identification experiment, in which a torque impulse was applied to the first cart and the oscillatory response of the second cart has been analyzed, has been initially performed. The
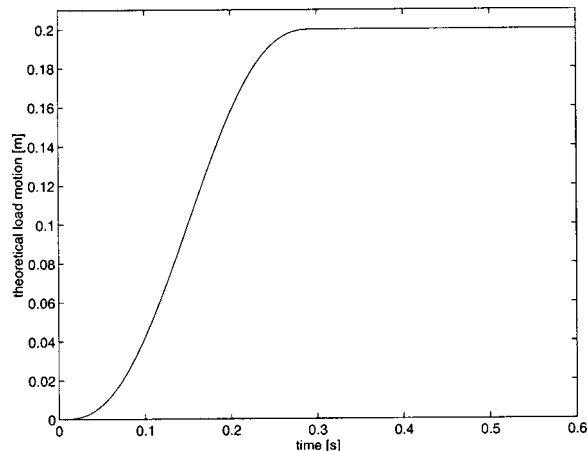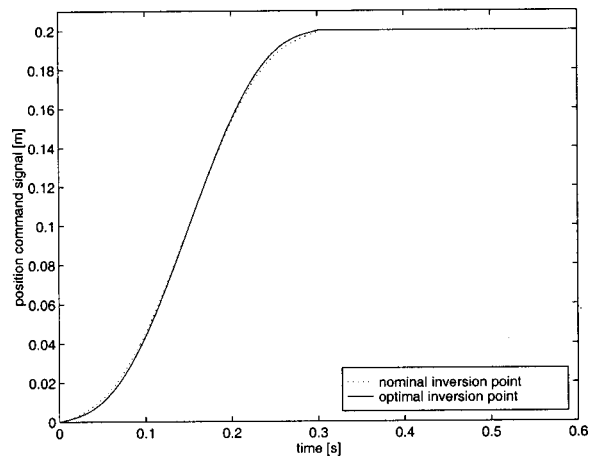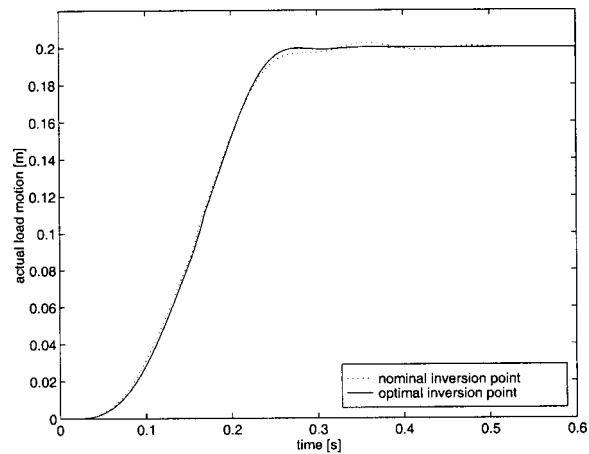

Fig. 4 The planned motion of the load

Fig. 5 The command input function for the nominal and optimal dynamic inversion

Fig. 6 The actual load motion for the nominal and optimal dynamic inversion

resulting values of k_0 and c_0 were 1858.15 kg·s^{-2} and 8.03 kg·s^{-1}, respectively, which corresponds to a nominal natural frequency of 48.19 rad·s^{-1} and a nominal damping ratio of 0.10. Then, a load motion of $q = 0.2$ m to be accomplished in $\tau = 0.3$ s was planned (see Fig. 4). The value of the motion time have been selected in order to exploit the full dynamics of the actuator, without saturating. A polynomial output function of fifth order ($h = 2$) has been adopted, in order to guarantee the continuity of the input function until the first order, i.e., discontinuities in the acceleration reference signal are allowed. Thus, we have:

$$x(t) = 0.2\left(\frac{6}{0.3^5} t^5 - \frac{15}{0.3^4} t^4 + \frac{10}{0.3^3} t^3 \right).$$

Then, the OIP procedure has been applied, having fixed $\delta_c = \delta_k = 10^{-4}$. At the end, it results in $k^* = 3000$ and $c^* = 0.001$, that is, a natural frequency of 61.24 rad·s^{-1} and a damping ratio of $1.02 \cdot 10^{-5}$. The resulting input function, obtained via dynamic inversion, is plotted in Fig. 5, where it is compared with the input function obtained by inverting the nominal system with k_0 and c_0. The actual load motions for both the nominal and optimal dynamic inversion are plotted in Fig. 6, where it appears that significant improvement is achieved by using the OIP procedure. Note that the objective function J is reduced from $2.7 \cdot 10^{-3}$ m to $0.6 \cdot 10^{-3}$ m. Moreover, the steady-state value of 0.2 m is attained at $t = 0.4$ s for the optimal case and at $t = 0.54$ s for the nominal one.

5 Conclusions

In this paper we have presented an important development in the system-inversion-based technique for the reduction of the residual vibration in point-to-point motion of mechanical servosystems endowed with elastic transmissions. It has been shown that the use of the dynamic inversion methodology provides flexibility in the motion planning design, as it allows to easily cope with the actuator limits. Moreover, the identification phase can be kept at a very simple level, as the use of the polynomial functions ensure an inherent robustness to the system and the OIP procedure allows achieving high performances straightforwardly. Indeed, despite the simple modeling of the system and the simple adopted optimization procedure, significant results have been obtained and the improvement with respect to the previously defined system-inversion-based methodology is evident. The readiness of the overall methodology makes it very suitable to be adopted in industrial environments, as demonstrated by the experimental results.

References

[1] Singer, N. C., and Seering, W. P., 1990, "Preshaping command inputs to reduce system vibration," ASME J. Dyn. Syst., Meas., Control, **112**, Mar., pp. 76–82.
[2] Singhose, W. E., Porter, L. J., Tuttle, T. D., and Singer, N. C., 1997, "Vibration reduction using multi-hump input shapers," ASME J. Dyn. Syst., Meas., Control, **119**, June, pp. 320–326.
[3] Piazzi, A., and Visioli, A., 2000, "Minimum-time system-inversion-based motion planning for residual vibration reduction," IEEE/ASME Trans. on Mech., **5**, No. 1, pp. 12–22.
[4] Piazzi, A., and Visioli, A., 2001, "Optimal noncausal set-point regulation of scalar systems," Automatica, **37**, No. 1, pp. 121–127.
[5] Adamini, R., Faglia, R., and Incerti, G., 1995, "Parametric motion planning techniques for servosystems endowed with elastic transmission," Machine Vibration, **4**, pp. 14–21.
[6] Luenberger, D. G., 1989, *Linear and Nonlinear Programming*, Addison Wesley, Reading.